

1 **Effects of spatial resolution on WRF v3.8.1 simulated meteorology over the central**
2 **Himalaya**

3 **Jaydeep Singh¹, Narendra Singh^{1*}, Narendra Ojha², Amit Sharma³, Andrea Pozzer^{4,5}, Nadimpally**
4 **Kiran Kumar⁶, Kunjukrishnapillai Rajeev⁶, Sachin S. Gunthe⁷, V. Rao Kotamarthi⁸**

5 ¹Aryabhata Research Institute of observational sciences (ARIES), Nainital, India

6 ²Physical Research Laboratory, Ahmedabad, India

7 ³Department of Civil and Infrastructure Engineering, Indian Institute of Technology Jodhpur, Jodhpur,
8 India

9 ⁴Department of Atmospheric Chemistry, Max Planck Institute for Chemistry, Mainz, Germany

10 ⁵Earth System Physics Section, International Centre for Theoretical Physics, Trieste, Italy

11 ⁶Space Physics Laboratory, Vikram Sarabhai Space Centre, Thiruvananthapuram, India

12 ⁷EWRE Division, Department of Civil Engineering, Indian Institute of Technology Madras, Chennai,
13 India

14 ⁸Environmental Science Division, Argonne National Laboratory, Argonne, Illinois, USA

15 **Correspondence:** Narendra Singh (narendra@aries.res.in) and Andrea Pozzer (andrea.pozzer@mpic.de)

16

17 **Abstract**

18 The sensitive ecosystem of the central Himalayan (CH) region, experiencing enhanced stress from
19 anthropogenic forcing, requires adequate atmospheric observations and an improved representation of the
20 Himalaya in the models. However, the accuracy of atmospheric models remains limited in this region due
21 to highly complex mountainous topography. This article delineates the effects of spatial resolution on the
22 modeled meteorology and dynamics over the CH by utilizing the Weather Research and Forecasting
23 (WRF) model extensively evaluated against the Ganges Valley Aerosol Experiment (GVAX) observations
24 during the summer monsoon. WRF simulation is performed over a domain (d01) encompassing northern

25 India at 15 km x 15 km resolution, and two nests: d02 (5 km x 5 km) and d03 (1 km x 1 km) centered over
26 CH with boundary conditions from respective parent domains. WRF simulations reveal higher variability
27 in meteorology, e.g. Relative Humidity (RH=70.3–96.1%), Wind speed (WS=1.1–4.2 ms⁻¹), as compared
28 to the ERA-Interim reanalysis (RH=80.0–85.0 %, and WS=1.2–2.3 ms⁻¹) over northern India owing to the
29 higher resolution. WRF simulated temporal evolution of meteorological variables, is found to agree with
30 the balloon-borne measurements with stronger correlations aloft ($r = 0.44–0.92$) than those in the lower
31 troposphere ($r = 0.18–0.48$). The model overestimates temperature (warm bias by 2.8°C) and
32 underestimates RH (dry bias by 6.4%) at the surface in d01. Model results show a significant improvement
33 in d03 (P=827.6 hPa, T=19.8 °C, RH=92.3%), closer to the GVAX observations (P=801.4 hPa, T=19.5
34 °C, RH=94.7%). Interpolating the output from the coarser domains (d01, d02) to the altitude of the station
35 reduces the biases in pressure and temperature, however, suppresses the diurnal variations but highlighting
36 the importance of well-resolved terrain (d03). Temporal variations in near-surface P, T and RH are also
37 reproduced by WRF in d03 to an extent ($r > 0.5$). A sensitivity simulation incorporating the feedback from
38 the nested domain demonstrates the improvement in simulated P, T and RH over CH. Our study shows
39 that the WRF model set up at finer spatial resolution can significantly reduce the biases in simulated
40 meteorology, and such an improved representation of CH can be adopted through domain feedback into
41 regional-scale simulations. Interestingly, WRF simulates a dominant easterly wind component at 1 km x
42 1 km resolution (d03), which is missing in the coarse simulations; however, the frequency of south-
43 easterlies remains underestimated. Model simulation implementing a high resolution (3s) topography input
44 (SRTM) improved the prediction of wind directions; nevertheless, further improvements are required to
45 better reproduce the observed local-scale dynamics over the CH.

46 **1. Introduction**

47 The Himalayan region is one of the most complex and fragile geographical systems in the world, and has
48 paramount importance for the climatic implications and air composition at regional to global scales (e.g.

49 Lawrence et al., 2010, Pant et al., 2018; Lelieveld et al., 2018). The ground-based observations of
50 meteorology and fine-scale dynamics are highly sparse and limited. In this direction, an intensive field
51 campaign known as the GVAX (Kotamarthi, 2013) was carried out over a mountainous site in the central
52 Himalaya which provided valuable meteorological observations for atmospheric research, model
53 evaluation and further improvements. Accurate simulations of meteorology are needed for numerous
54 investigations, such as to study the regional and global climate change, snow-cover change, trapping and
55 transport of regional pollution, and the hydrological cycle, especially the monsoon system (e. g. Sharma
56 and Ganju, 2000; Bhutiyani et al., 2007; Pant et al., 2018). Studies focussing over this region have become
57 more important due to the increasing anthropogenic influences resulting in enhanced levels of Short-Lived
58 Climate forcing Pollutants (SLCPs) along the Himalayan foothills (e. g. Ojha et al., 2012; Sarangi et al.,
59 2014; Rupakheti et al., 2017; Deep et al., 2019; Ojha et al., 2019). Although Global Climate Models
60 (GCMs) simulate the climate variabilities over global scale, their application for reproducing observations
61 in the regions of complex landscapes is limited, due to coarse horizontal resolution (e. g. Wilby et al.,
62 1999; Boyle et al. 2010; Tselioudis et al., 2012; Pervez and Henebry, 2014; Meher et al., 2017). Mountain
63 ridges, rapidly changing land-cover, and the low altitude valleys often lie within a grid box of typical
64 global climate models resulting in significant biases in model results when compared with observations
65 (e. g. Ojha et al., 2012; Tiwari et al., 2017, Pant et al., 2018). On the other hand, Regional Climate Models
66 (RCMs) at finer resolutions allow better representation of the topographical features, thus providing
67 improved simulations of the atmospheric variability over regions of complex terrain. Several mesoscale
68 models (e. g. Christensen et al., 1996; Caya and Laprise 1999; Skamarock et al., 2008; Zadra et al., 2008)
69 have been developed and applied successfully over different parts of the world. These studies have
70 revealed that the RCMs provide significantly new insights by parameterizing or explicitly simulating
71 atmospheric processes over finer spatial scales. Nevertheless, large uncertainties are still seen over highly
72 complex areas indicating the effects of further unresolved terrain features (e. g. Wang et al., 2004; Laprise,
73 2008; Foley, 2010) and need to improve the simulations.

74 Anthropogenic influences and climate forcing have been increasing over the Himalaya and its foothill
75 regions since pre-industrial times (Bonasoni et al., 2012; Srivastava et al., 2014; Kumar et al., 2018).
76 Consequently, an increase in the intensity and frequency of extreme weather events has been observed
77 over the Himalayan region (e. g. Nandargi and Dhar, 2012; Sun et al., 2017; Dimri et al., 2017) in the past
78 few decades. These events include extreme rainfall and resulting flash floods, cloudbursts, landslides etc.,
79 and the associated weather systems range from mesoscale to synoptic-scale phenomena. Unfortunately,
80 the lack of an observational network covering the Himalaya and foothills with sufficient spatio-temporal
81 density inhibits the detailed understanding of the aforementioned processes, meteorological and dynamical
82 conditions in the region. Therefore, usage of regional models, evaluated against available in-situ
83 measurements can fill the gap of investigating atmospheric variability in the observationally sparse and
84 geographically complex mountain terrain of the Himalaya.

85 The biases in simulating the meteorological parameters especially in the lower troposphere are associated
86 with several factors, e.g. representation of topography, land use, surface heat and moisture flux transport,
87 and parameterization of physical processes (e. g. Lee et al., 1989; Hann and Yang, 2001; Cheng and
88 Steenburgh, 2005; Singh et al., 2016). The WRF has been used for the model experiments over complex
89 terrain around the world, e.g., the Himalaya region (e.g. Sarangi et al., 2014; Singh et al., 2016, Mues et
90 al., 2018; Potter et al., 2018; Norris et al., 2020; Wang et al., 2020), Tibetan Plateau (e.g. Gao et al., 2015;
91 Zhou et al., 2018), and the multiple mountain ranges in the western United States (e.g. Zhang et al., 2013)
92 to evaluate and study the meteorology and dynamics. A cold bias was reported in this model over the
93 Tibetan Plateau and the Himalayan region by Gao et al (2015). The near-surface winds showed biases
94 linked with unresolved processes in the model such as sub-grid turbulence, land-surface atmospheric
95 interactions, besides boundary layer parametrization (Hanna and Yang, 2001; Zhang and Zheng, 2004;
96 Cheng and Steenburgh, 2005). Zhou et al (2018) found lower biases in simulated winds after considering
97 the turbulent orographic formed drag over the Tibetan Plateau.

98 The WRF model with suitably chosen schemes has been shown to reproduce the regional-scale
99 meteorology (Kumar et al., 2012) and to some extent also the mountain-valley wind systems (Sarangi et
100 al., 2014) and boundary layer dynamics (Singh et al., 2016; Mues et al., 2018) over the Himalayan region.
101 Nevertheless, local meteorology is still difficult to simulate accurately; Mues et al (2018) performed high-
102 resolution WRF simulation over the Kathmandu valley of Himalaya and reported overestimation of 2m
103 temperature and 10m wind speed, which they attributed to insufficient resolution of the complex
104 topography, even at a resolution of 3 km. Although few studies have used the WRF model at very high
105 resolution over the Himalayan region (e.g., Cannon et al., 2017; Mues et al., 2018; Potter et al., 2018;
106 Zhou et al., 2018; Zhou et al., 2019; Norris et al., 2020; Wang et al., 2020), still the model performance
107 over the complex terrains like the Himalaya requires improvement which can be done through an extensive
108 evaluation at sub-kilometer resolution against an intensive field campaign. The main objectives of the
109 study are as follows:

- 110 1. To examine the model performance over the CH at varying resolutions (15km, 5km and 1km) by
111 evaluating several model diagnostics against the observations made during the GVAX campaign.
- 112 2. To investigate the effect of feedback from nest to the parent domain, as this might allow
113 configuring a model setup covering the larger Indian region with more accurate results over the
114 Himalaya
- 115 3. The downscaling to a sub-kilometer (333m) resolution with the implementation of a very high
116 resolution (3 s) topographical input into the model to examine the potential of simulations in
117 reproducing local-scale dynamics

118 The subsequent section 2 describes the model set up, followed by experimental design, and a discussion
119 of datasets used for model evaluation. Section 3 provides a comparison of model results with the ERA-
120 Interim reanalysis (section 3.1), radiosonde observations (section 3.2), and ground-based measurements
121 (section 3.3). Analysis of domain feedback is presented in section 3.4, and the effect of implementing

122 high-resolution topography is investigated in section 3.5, followed by the summary and conclusions in
123 section 4.

124 **2. Methodology**

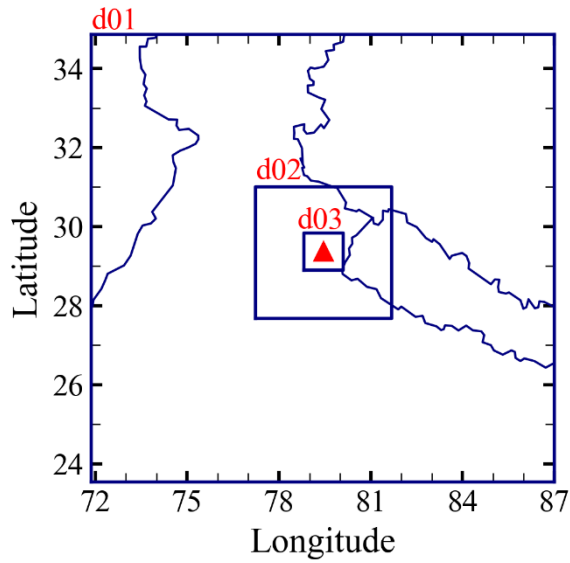
125 **2.1 Model set up and Experimental Design**

126 The WRF model—version 3.8.1 has been used in the present study. WRF is a mesoscale non-hydrostatic,
127 Numerical Weather Prediction (NWP) model with advance physics and numerical schemes for simulating
128 meteorology and dynamics. WRF-ARW uses an Eulerian mass-based dynamical core with terrain-
129 following vertical coordinates (Skamarock et al., 2008). ERA-Interim reanalysis from the European Center
130 for Medium-Range Weather Forecasts (ECMWF) available at a temporal resolution of 6 hour and
131 horizontal resolution of $0.75^0 \times 0.75^0$ with 37 vertical levels from the surface to the top at 1 hPa (Dee et
132 al., 2011), has been used to provide the initial and lateral boundary conditions to the WRF model. Static
133 geographical data from Moderate Resolution Imaging Spectroradiometer (MODIS) available at 30s
134 horizontal resolution, is utilized for land use, and land cover.

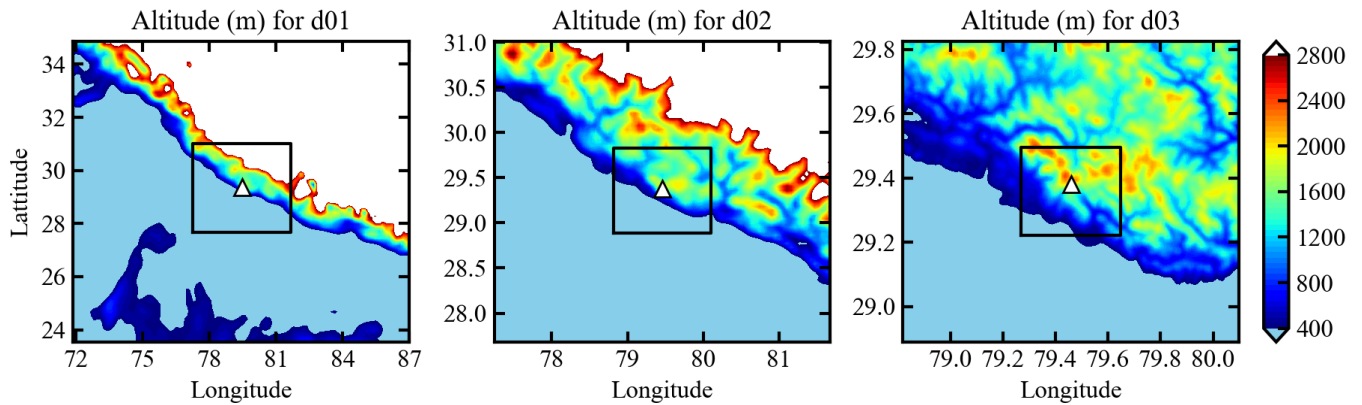
135 The Goddard scheme is used for shortwave radiation (Chou and Suarez, 1994), while the longwave
136 radiation is simulated by the Rapid Radiative Transfer Model scheme (Mlawer et al., 1997). For resolving
137 the boundary layer processes the first order non-local closure based Yonsei University (YSU) scheme
138 (Hong et al., 2006) is used including an explicit entrainment layer with the K-profile in an unstable mixed
139 layer. PBL height is determined from the Richardson number (Ri_b) method in this PBL scheme.
140 Convection is parameterized by the Kain-Fritsch (KF) cumulus parameterization (CP) scheme, accounting
141 for sub-grid level processes in the model such as precipitation, latent heat release and vertical redistribution
142 of heat and moisture as a result of convection (Kain, 2004). With the increase in model grid resolution to
143 less than 10 km (known as “grey area”), the CP scheme is usually turned off, and cloud and precipitation
144 processes are resolved by the microphysics (MP) scheme (Weisman et al., 1997). In the present study, the
145 CP scheme is used for d01 while it is turned off for d02 and d03. The Thomson microphysics containing

146 prognostic equations for cloud water, rainwater, ice, snow, and graupel mixing ratios, is used (Thompson
147 et al., 2004). Parameterization of surface processes is done with MM5 Monin-Obukhov scheme and
148 Unified Noah land surface model (LSM) (Chen and Dudhia, 2001; Ek et al., 2003; Tewari et al., 2004).
149 The Noah LSM includes a single canopy layer and four soil layers at 0.1, 0.2, 0.6 and 1m within 2m of
150 depth (Ek et al., 2003).

151 The model is configured with three domains of 15 km (d01), 5 km (d02) and 1 km (d03) horizontal grid
152 spacing using Mercator projection centering at Manora Peak (79.46°N, 29.36°E, amsl ~ 1936m) in the
153 central Himalaya. The topography within the model domains is highly complex, as evident from the ridges
154 (Figure 1). The outer domain d01 includes the northern part of Thar Desert, part of Indo-Gangetic Plain
155 (IGP), and the Himalayan mountains, while the innermost domain d03 consists of mostly mountainous
156 terrain. The model has 51 atmospheric vertical levels with the top at 10 hPa. For d01, 100 east-west and
157 86 north-south grid points are used to account for the effect of synoptic-scale meteorology, e.g. Indian
158 summer monsoon. The d02 has 88 east-west and 76 north-south grid points covering sufficient spatial
159 region around the observational site to consider the effects of mesoscale dynamics, e.g. change of wind
160 pattern due to orography. The innermost domain, d03, has 126 east-west and 106 north-south grid points
161 to resolve local effects, e.g. convection, advection, turbulence, and orthographic lifting.



162



163

164 **Figure 1:** Topography represented in the WRF model domains with three horizontal resolutions, namely-
 165 domain d01 (15 x 15km), domain d02 (5 x 5km) and domain d03 (1 x 1 km). Each box inside corresponds
 166 to the nested domain (upper panel). Triangle in the innermost box indicates the location of the GVAX-
 167 campaign site i.e. Manora peak Nainital. Bottom panel belongs to the topography of each individual
 168 domain (left to right). The finest nest inside of the d03 (bottom right) is d04 at the resolution of 333m
 169 (discussed in section3.5)

170 For d01, boundary conditions are provided from ERA-Interim reanalysis, as explained earlier. Model
 171 simulations have been performed for the four months of summer monsoon: 1 June 2011 to 30 September
 172 2011 (JJAS). This simulation period is chosen considering the availability of continuous observations from

173 11 June 2011 and to allow sufficient spin-up time of 10 days for the model to achieve its equilibrium state
174 (Angevine et al., 2014; Seck et al., 2015; Jerez et al., 2020). Only, the outer domain d01 is nudged with
175 the global reanalysis for temperature, water vapor, zonal and meridional (u and v) components of wind
176 using nudging coefficient of 0.0006 (6×10^{-4}) at all vertical levels (e.g. Kumar et al., 2012). Several of the
177 configuration options e. g. physics and meteorological nudging are selected following earlier applications
178 of this model over this region (e. g. Kumar et al., 2012; Ojha et al., 2016; Singh et al., 2016; Sharma et al.,
179 2017).

180

181 **2.2. Observational data**

182 We utilize the observations conducted during an intensive field campaign- the Ganges Valleys Aerosol
183 Experiment (GVAX) to evaluate model simulations. The GVAX campaign was carried out using
184 Atmospheric Radiation Measurement (ARM) Climate Research Facility of the U.S. Department of Energy
185 (DOE) from 10 June 2011 to 31 March 2012 at ARIES, Manora Peak in Nainital (e.g. Kotamarthi, 2013;
186 Singh et al., 2016; Dumka et al., 2017). This observational site (79.46°N, 29.36°E, 1940m above sea level)
187 is located in the central Himalaya, as shown in Figure 1. The surface-based meteorological measurements
188 of ambient air temperature, pressure, relative humidity, precipitation, wind (speed and direction) were
189 made using an automatic weather station at 1-minute temporal resolution. The instantaneous values of the
190 observations are compared with hourly instantaneous model output at the nearest grid point.

191 The vertical profiles of temperature, pressure, relative humidity and horizontal wind (speed and direction)
192 were obtained by four launches (00:00, 06:00, 12:00 and 18:00 UTC) of the radiosonde each day during
193 the campaign (Naja et al., 2016). The continuous vertical profiles of the meteorological parameters except
194 wind speed and direction were available from the end of June 2011 to the entire study period, whereas
195 valid and quality wind data were available only for September 2011. Hence, in this study, radiosonde
196 measurements from 1 July 2011 onwards are used for the model evaluation of meteorological parameters,

197 except wind speed and direction, which are evaluated only for September. A total of 309 valid profiles of
198 temperature and relative humidity and 104 profiles of wind are used. The statistical metrics such as mean
199 bias (MB), root mean square error (RMSE) and correlation coefficient (r) are used for the model
200 evaluation, and the description of these metrics is given in the supplementary material.

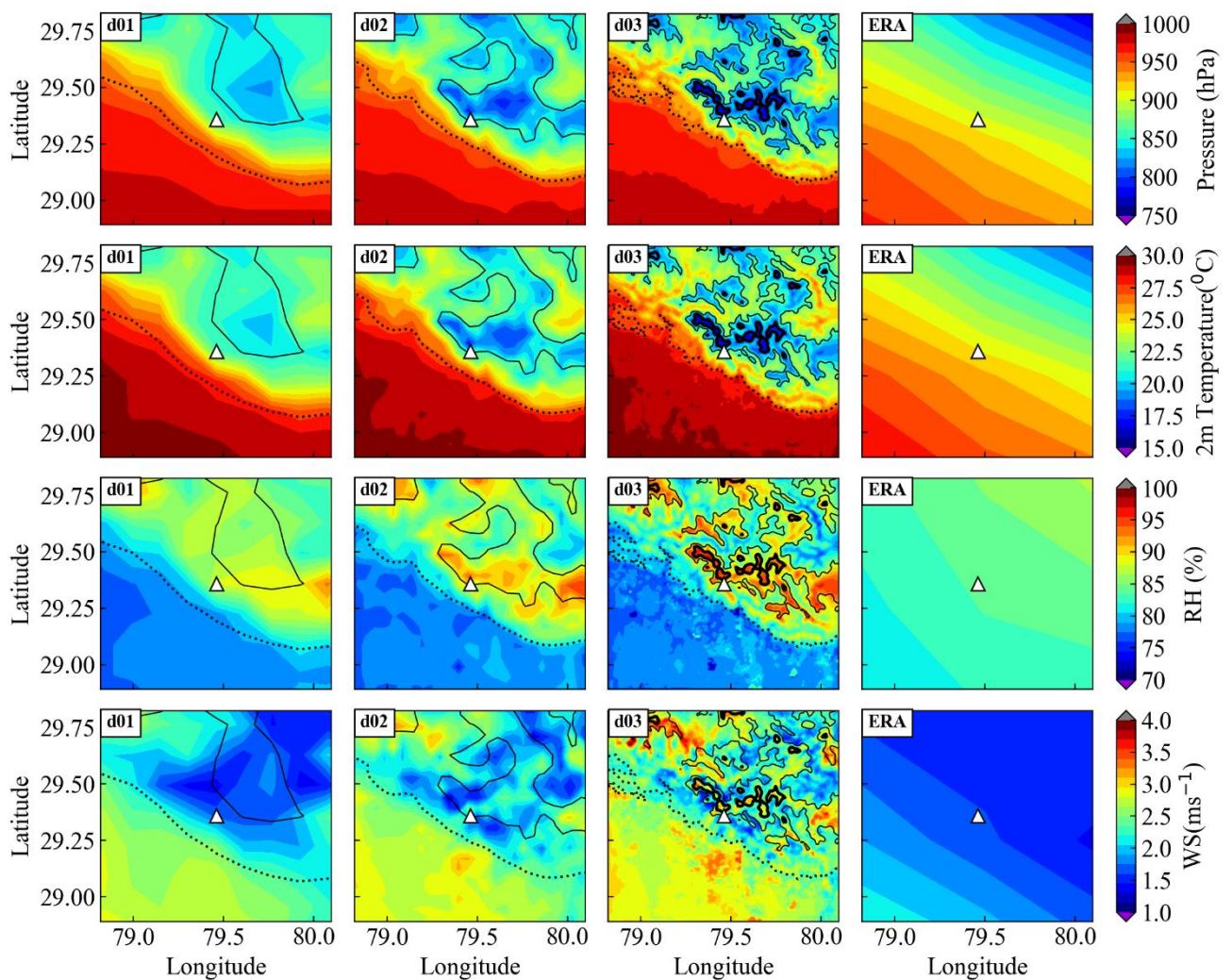
201

202 **3. Results and Discussions**

203 **3.1. Comparison with ERA-Interim reanalysis**

204 Here, we have used the ERA-Interim data for comparison with WRF output. We first compare the WRF
205 simulated spatial distribution of meteorological parameters (surface pressure, 2m air temperature, 2m RH
206 and 10m WS) with ERA-Interim reanalysis over the common region of all the domains and averaged for
207 the entire simulation period (Figure 2). The three contours of the topographic height of 500m, 1500m and
208 2000m are used to relate the meteorological features to the resolved topography in three domains. The
209 common area in all domains includes low-altitude IGP region in the south (elevation of less than 400m,
210 Figure 1) and elevated mountains of central Himalaya in the north. Also, for a consistent comparison,
211 model simulated values are taken at the same time intervals as that in ERA-Interim data (i.e. every 6h).
212 From the comparison presented in Figure 2, it is evident that the meteorological parameters simulated by
213 the model are dependent on the model grid resolution. The existence of the sharp gradient topographic
214 height (SGTH) of about 1600 m from the foothill of the Himalaya to the observational site modifies the
215 wind pattern as well as moisture content differently at different grid resolutions, indicating the critical role
216 of mountain orography. The surface pressure explicitly depends upon the elevation of a location from
217 mean sea level. The contour of the pressure parameter from ERA-Interim data shows the surface pressure
218 of about 900hPa for observational site Manora Peak and varied from 550 to 975 hPa within this region,
219 while WRF simulated pressure is 869 hPa, 835hPa and 827 hPa for d01, d02 and d03, respectively. WRF
220 simulated surface pressure ranges from 821.9 hPa over high altitude CH region to 977.0 hPa in IGP region

221 within d01. Simultaneously, the range of variation in the surface pressure is 788.1 – 977.5 and 760.4–
 222 977.7 hPa within d02 and d03 respectively, and the minimum pressure decreases from d01 to d03 which
 223 is attributed to the improvement in resolved topography on increasing model grid resolution. However,
 224 the effects of the SGTH are not observed for temperature, wind and RH in ERA-Interim contours, due to
 225 the unresolved topographic features. Simulated maps show spatial homogeneity of meteorological
 226 parameters over the flat terrain of IGP in the foothills of Himalaya as compared to elevated central
 227 Himalayan region.



228
 229 **Figure 2.** Contours in the first three columns show WRF results for the three domains (first column: d01,
 230 second column: d02 and third column: d03) and the fourth column shows corresponding parameters from
 231 the ERA-Interim reanalysis. First row shows mean surface pressure during the monsoon (JJAS), the

232 second row shows 2m temperature (in $^{\circ}\text{C}$), 3rd row shows 2m relative humidity (RH; %) and the bottom
233 row shows 10 m wind speed (WS; ms^{-1}) along with three elevation contours at 500m (dashed), 1500m
234 (thin solid), and 2000m (thick solid).

235 The effect of spatial resolution is clearly observed over the mountainous region of the Himalaya, where
236 the size of the mountains changes abruptly, with the modelled output showing increasingly distinct features
237 with increasing grid resolution. On the other hand, there are minimal differences in the topography of the
238 IGP, and hence the meteorological features associated with the topography are well captured in the model
239 even at a coarser resolution of 15 km.

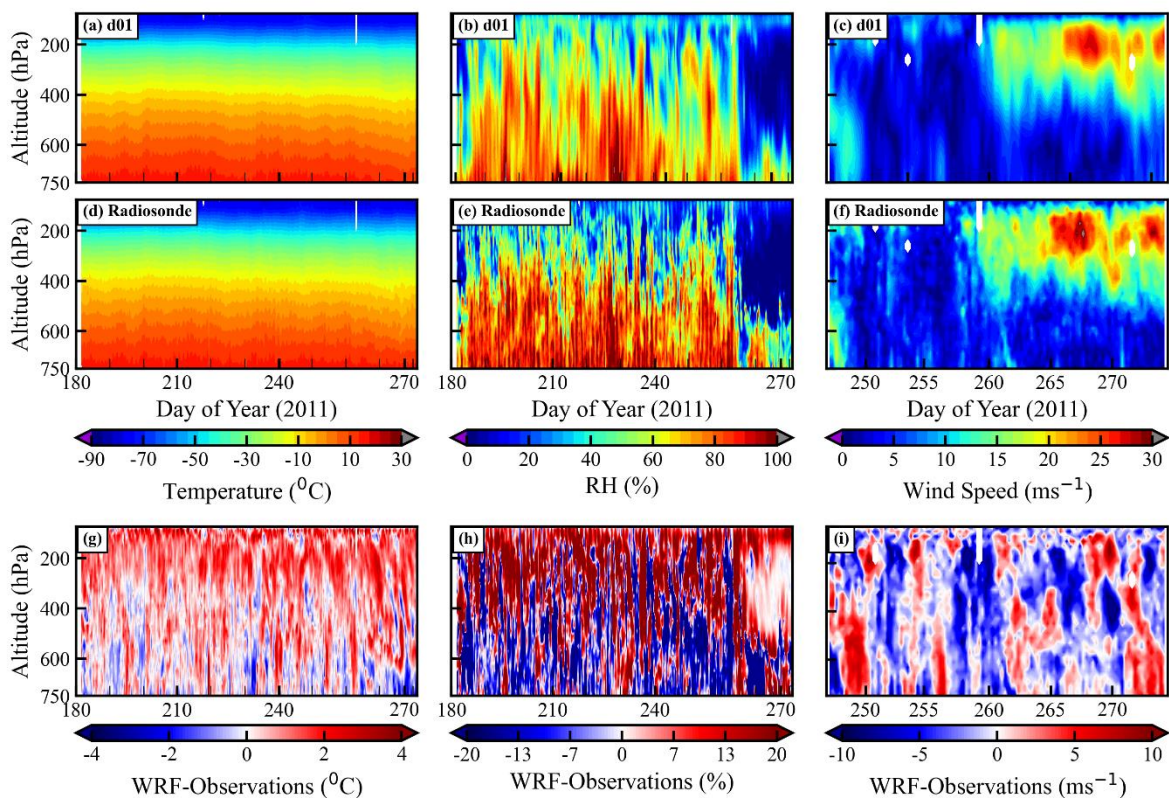
240 Model simulations show the topography dependent spatial variation in 2m temperature in the ranges of
241 $20.0\text{--}29.5^{\circ}\text{C}$ in d01, $17.3\text{--}29.6^{\circ}\text{C}$ in d02, and $15.5.0\text{--}29.9^{\circ}\text{C}$ in d03, with lowest values simulated over the
242 elevated mountain peaks and higher values over the temperate IGP region. The contours in three model
243 domains show an explicit dependency of 2m temperature on the grid resolution over the mountainous
244 region. With the increasing model resolution, the topography is resolved to a greater extent, and lower
245 temperature is simulated at higher surface elevations, as expected. Further, the estimation of water vapour
246 is essentially needed for both climate and numerical weather prediction (NWP) applications. Figure 2
247 shows that the simulated relative humidity is above 70% in all three domains for the monsoon season. The
248 variations (minimum-maximum) in the relative humidity in ERA-Interim (80% - 85%) data set, over the
249 domains d01 (77-93%), d02 (74 - 95%), and d03 (70- 96%) are generally comparable. The mountain
250 slopes provide the uplift to the moist monsoonal air that on ascent subsequently saturates and increases
251 the relative humidity to about 90% as observed over the grid encompassing the site. Contour lines (1500m
252 and 2000m in Figure 2) depict the low pressure and temperature with the higher relative humidity feature
253 of the peaks and these features are sharper as the resolution increases from d01 to d03.

254 The wind speed is highly dependent upon the model grid resolution as well as orography-induced
255 circulations during different seasons (Solanki et al., 2016; 2019), and reflected by Figure 2. As mentioned

256 earlier, although the topography of the IGP region does not vary abruptly, the magnitude of the wind speed
 257 over this region as well as over the complex Himalayan region is found to change significantly at different
 258 model resolutions, thereby, indicating that the wind speed is very sensitive to both model resolution and
 259 topography. The wind speed in d01 varies from 1.3 ms^{-1} to 2.8 ms^{-1} , while the wind variations in domains
 260 d02 ($1.2 - 3.4 \text{ ms}^{-1}$) and d03 ($1.3 - 4.2 \text{ ms}^{-1}$) show higher variability than that in the ERA-interim ($1.2-$
 261 2.3 ms^{-1}) due to finer resolution of the WRF. Overall, the impact of the topography resolved at higher
 262 resolution in WRF shows the contrasting differences in surface pressure, temperature, relative humidity
 263 and wind speed compared to coarse resolution ERA-interim dataset.

264 3.2. Comparison with Radiosonde observations

265 The intensive radiosonde observations made during the GVAX field campaign at Manora Peak (79.46°N ,
 266 29.36°E , amsl $\sim 1936\text{m}$) in the central Himalaya (shown in Figure 1) are used for the evaluation of model
 267 resolutions. The comparison of the model simulated profiles of temperature, relative humidity, and wind
 268 speed against the radiosonde observations are shown in Figure 3.



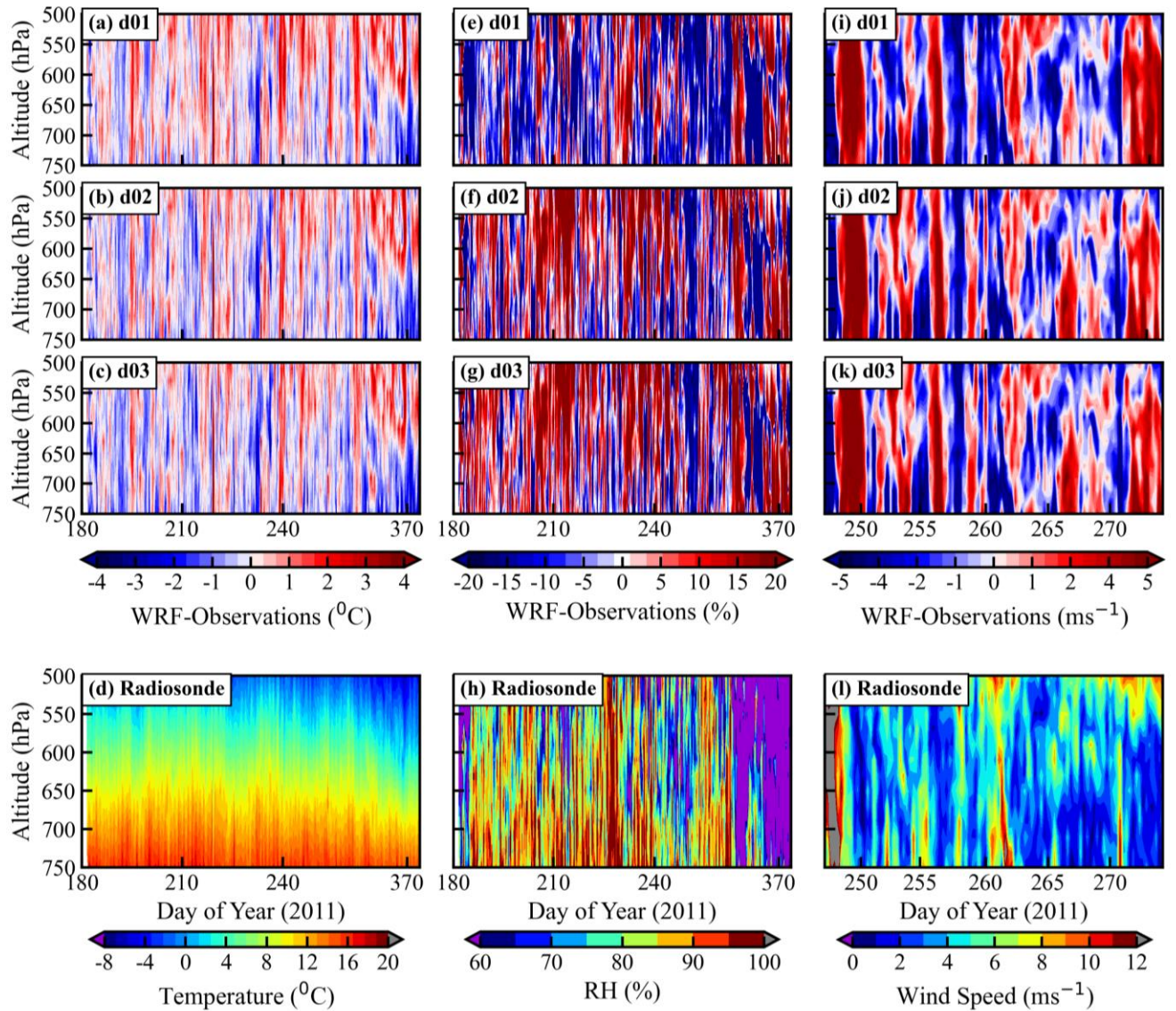
269

270 **Figure 3:** The comparison of simulated vertical profiles of (a) temperature ($^{\circ}\text{C}$), (b) relative humidity
271 (RH; %), and (c) wind speed (ms^{-1}) in d01 with the radiosonde observations (d, e, and f). The x-axis of
272 (a), (b), (d), (e), (g) and (h) show the day of the year 2011 starting from 1 July (182nd day) to 30 September
273 (273rd day). The vertical profiles of wind speed (c, f) are plotted only for September 2011. The third row
274 (g, h, and i) shows the difference in temperature, relative humidity, and wind speed, between WRF d01
275 simulation and radiosonde observation.

276 The inversion of temperature at the top of the troposphere occurred at $\sim 90\text{hPa}$ ($\sim 16\text{km}$) in observations
277 (Figure 3d, Figure S1) whereas, radiosonde profiles show that temperature decreases with pressure from
278 15.5°C at 750 hPa to -78.0°C at $\sim 90\text{ hPa}$. As evident from the simulated temperature profiles, the WRF
279 model well captured these features and found to show a reduction from 15.1°C to -76.6°C in these pressure
280 levels. Further, the differences between model (d01) and radiosonde observations (Figure 3g) range from
281 -4 to 4°C . The mean RH values from the radiosonde observations (model d01) also show decrease from
282 82.3% (76.7%) at 750 to 25.2% (32.0%) at 90 hPa . The mean RH difference between observation and
283 model (Figure 3h) shows that the model simulates more humid atmosphere at higher altitudes while
284 showing a low-humidity bias in lower altitudes. The wind data from radiosonde measurements available
285 for September 2011, were utilized to compare the model output. Observations and modelled winds are
286 $\leq 10\text{ ms}^{-1}$, within the altitude region of the surface to about 400hPa ($\sim 7\text{ km}$) till mid of September (day of
287 the year 258). Wind increases ($\geq 15\text{ ms}^{-1}$) above 400 hPa and attains maximum values ($\geq 25\text{ ms}^{-1}$) between
288 250 and 100hPa after 258 day of the year (15th September 2011). However, simulated winds are slightly
289 lower and less wide spreads as compared to observations. The comparison of the wind profiles with the
290 same x-axis (shown in Figure S2) with other meteorological parameters show that the lower relative
291 humidity ($<30\%$) is observed along with higher wind speed during this period. In general, the vertical
292 profiles and variation of simulated wind speed agree well with the observation. The Taylor diagram
293 (Taylor, 2001), in Figure 7a, is used to express the statistical comparison between model simulations and
294 observations. In the diagram, the comparison is summarized with correlation coefficient (r), normalized

295 root mean squared difference (RMSD) and standard deviation, normalized by that of the observations
296 (SD). In most cases, the model simulates less variability in meteorological parameters as shown by the
297 normalized standard deviation, which is less than 1. For temperature and wind speed, model shows good
298 correlation (r) with the observations at 250hPa ($r > 0.80$) than that in lower altitudes i.e. 750hPa ($r < 0.40$).
299 On the other hand, the model captures variability in humidity relatively well at 500 hPa ($r = 0.71$) but
300 shows poor correlation at 75 hPa ($r = 0.17$) near the model top.

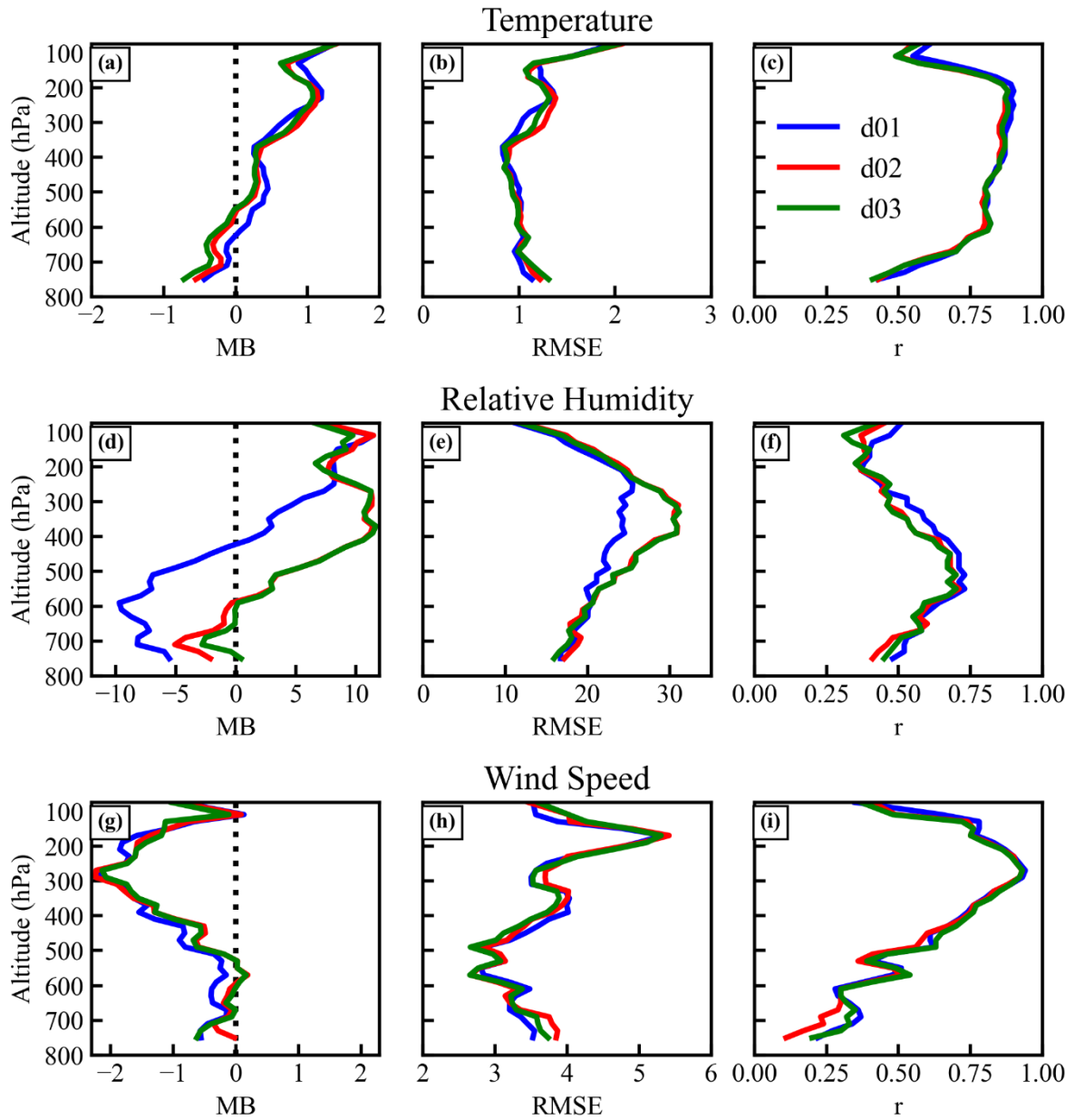
301 Lower correlations for temperature and wind speed near to the surface (750 hPa) could be due to the terrain
302 induced effects which are most significant in the local boundary layer. The surface-level winds and
303 turbulence are some of the boundary layer features, affected mainly by the surface and terrain
304 characteristics. The vertical profiles of these parameters up to 500 hPa in all three model domains are
305 shown in Figure 4. Differences between the simulated vertical profile of temperature and radiosonde
306 observation are in general similar in all the domains. Except for the relative humidity in d01, other
307 meteorological parameters (temperature and wind speed) do not reveal strong dependencies on the model
308 resolution. However, the model overestimates the relative humidity near 500hPa level in d02 and d03 on
309 some of the days. In case of the wind speed, the model underestimates the magnitude of the wind in the
310 first few days up to 500 hPa, though by and large the model is able to capture the vertical profiles.



311
 312 **Figure 4:** Difference between model (d01: first row, d02: second row, d03: third row) and radiosonde
 313 observation for temperature (first column: a, b, c), relative humidity (second column: e, f, g) and wind
 314 speed (third column: i, j, k) profiles up to 500 hPa. The fourth row provides the vertical profiles of
 315 radiosonde measurements. The x-axis of the panels (a-h) shows the day of the year 2011 from 1 July (182nd
 316 day) to 30 September (273rd day). Wind speed (ms^{-1}) profiles in the panels (i-l) are provided for September
 317 2011.

318 Figure 5 shows the vertical profiles of the statistical metrics: mean bias (MB), root mean square error
 319 (RMSE), and correlation coefficient (r) for temperature, relative humidity, and wind speed for the three
 320 simulations (d01, d02, d03). The magnitudes of the MB values throughout the troposphere are estimated

321 to be within about 1 °C, 12 %, and 2.5 ms⁻¹ for temperature, relative humidity, and wind speed,
322 respectively. Additionally, RMSE values are about 1 °C, 15–30%, and 2.5–5 ms⁻¹ for temperature, relative
323 humidity, and wind speed, respectively. As discussed earlier, correlations between model results and
324 observations are found to be stronger in the middle and upper troposphere than in the lower troposphere.
325 For temperature, the r values are higher than 0.75 between 600 to 200 hPa, whereas it decreases up to 0.4
326 at lower altitudes, i.e. near 800 hPa. Correlations in the lower troposphere are notably weaker (r = ~0.25)
327 in case of wind speed. The results suggest that the model captures well the day-to-day variabilities in the
328 meteorological parameters in the middle and upper troposphere and to a minor extent in the lower
329 troposphere. Relatively weaker correlations in the lower troposphere are suggested to be associated with
330 more pronounced effects of the uncertainties caused by the underlying complex mountain terrain and
331 resulting unresolved local effects. Wind fields near the surface are strongly impacted by interactions
332 between terrain and boundary layer besides orographic drag in a modelling study over the Tibetan Plateau
333 (Zhou et al., 2018) and in measurements over the Himalaya (Solanki et al., 2019). Increase in bias with
334 altitude was reported by Kumar et al (2012) for dew point temperature. Besides the model physics, the
335 higher uncertainties in radiosonde humidity observations might have also contributed to these differences.
336 The effect of model resolution is not very significant for temperature and wind profiles above 800 hPa;
337 nevertheless, the mean bias for RH is lower (~5%) in the 800–600 hPa altitude range and higher in the
338 450–300 hPa altitude range in the d02 and d03 simulations. This might be arising due to deep convection
339 in the model at a higher resolution. Overall, the model captured the vertical structures of meteorological
340 parameters; however, better representation of complex terrain itself is insufficient for improving the model
341 performance aloft. On top of the, better representation of topography as considered here, it highlights the
342 need for future studies evaluating various physics scheme. Nevertheless, model biases have been
343 significantly reduced for surface level meteorology with higher resolution, and the details are discussed in
344 the subsequent section.



345

346 **Figure 5.** The vertical profiles of mean bias (MB), root mean square error (RMSE), and correlation
 347 coefficient (r) for temperature, relative humidity, and wind speed for different domains d01 (blue), d02
 348 (red) and d03 (green).

349

350 3.3. Comparison with ground-based observations

351 The model simulated 2m temperature (T2), 2m relative humidity (RH2) and 10 m wind speed (WS10) for
 352 the observational site, Manora Peak are compared with the ground-based measurements made during

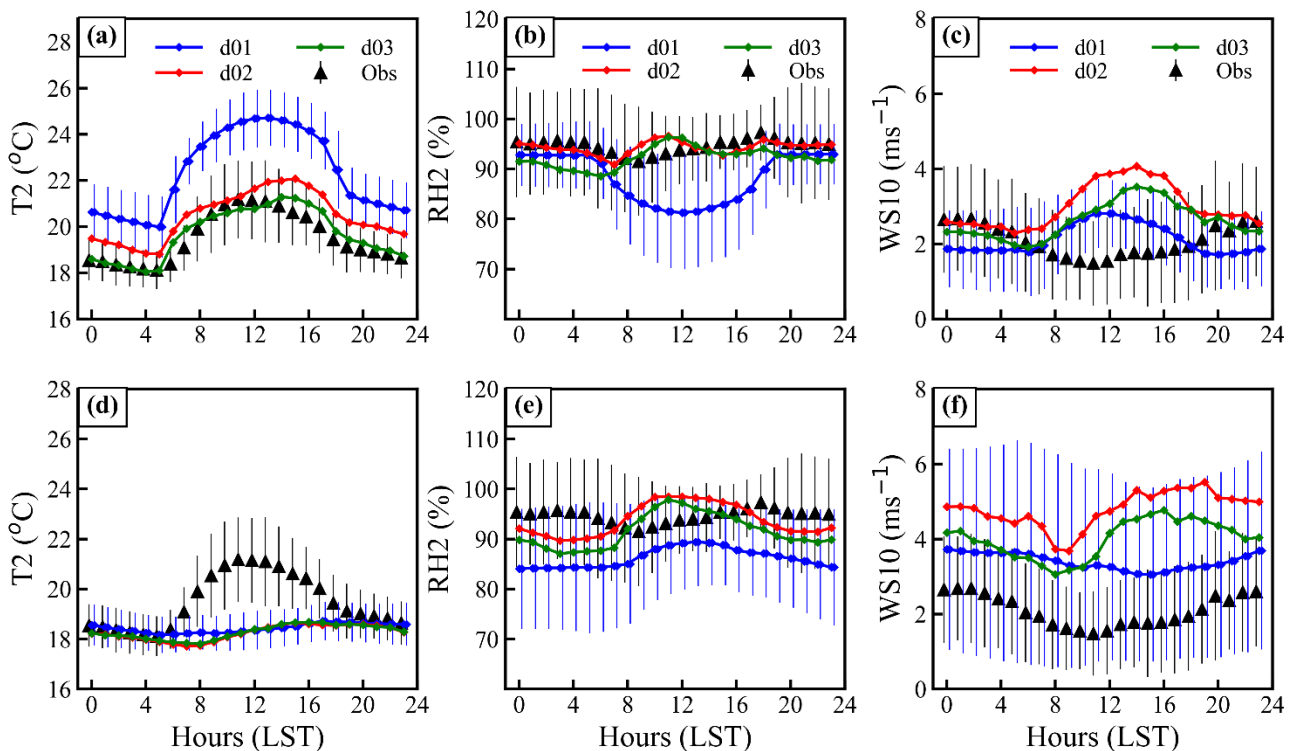
353 GVAX campaign in Figure 6 and summarized in Table 1. The diurnal variations in T2, RH2 and WS10
354 simulated by the WRF model are compared with observations, whereas the surface pressure does not show
355 a significant diurnal variation (not shown here). Model simulation d01 shows a positive bias of 68 hPa in
356 surface pressure with strong correlation ($r = 0.97$) with observation (mean = ~ 801 hPa). A significant
357 improvement is achieved (MB = 26 hPa) in d03 as a result of the finest resolution simulation (Figure 6
358 and Table 1). The WRF model simulated T2 shows warm bias in all three domains. The simulated T2 for
359 d01 varies from 16.2 to 28.7 $^{\circ}\text{C}$ with the higher mean value of $22.3 \pm 2.1^{\circ}\text{C}$ as compared to the observed
360 mean value of $19.5 \pm 1.6^{\circ}\text{C}$ with a correlation of $r = 0.75$ between d01 and observation. This warm bias is
361 seen to decrease from d01 (2.8 $^{\circ}\text{C}$) with the increasing model resolution to 0.2 $^{\circ}\text{C}$ in d03 simulation (Table
362 S1). The mean value of the RH2 in d01 is about $88.2 \pm 9.7\%$, 6.4% lower than the observed value $94.7 \pm 9.5\%$
363 with the correlation about 0.45 (Figure 7b). MB and RMSE values of RH2 show a decrease with increasing
364 model resolution (Table S1). As relative humidity also depends on temperature; therefore, the diurnal
365 variation in 2m specific humidity (Q2; g kg^{-1}) has also been analyzed (Figure S3). Q2 is observed in the
366 range of 5.5–21.5 g kg^{-1} with the mean value as $16.8 \pm 2.0 \text{ g kg}^{-1}$. It is found that the agreement in Q2 is
367 relatively better (MB = -0.7 g kg^{-1} ; $r = 0.77$ in d03), when the statistical metrics are compared with that
368 for RH2 (Table S1). The wind speed plays a vital role in transport processes and controls the dynamics of
369 the atmosphere at different temporal and spatial scales. The average 10m wind speed (WS10) during
370 monsoon over the measurement station is about $2.1 \pm 1.4 \text{ ms}^{-1}$ which is quite comparable to that simulated
371 in d01 ($2.1 \pm 1.1 \text{ ms}^{-1}$) whereas overestimated in d02 by 0.9 ms^{-1} and in d03 by 0.5 ms^{-1} (Table 1 and Table
372 S1). In the case of the WS10, the correlation is 0.18 for d01 and d02, which improves to 0.24 in d03. The
373 diurnal variation of WS10 (Figure 6c) is not well captured, especially during the noontime.

374 **Table 1:** Mean (\pm Standard deviation) along with the minimum and maximum values of the meteorological
375 parameters: surface pressure (P; hPa), 2m Temperature (T2; $^{\circ}\text{C}$); 2m relative humidity (RH2; %) and 10m
376 wind speed (WS10; ms^{-1}) in the model simulations and observations for the full observation period. An

377 additional evaluation is presented, accounting for the difference in model surface altitude and actual
 378 altitude of measurements (referred to as ‘With altitude adjustment’).

Parameter	Without altitude adjustment			With altitude adjustment			Observation
	d01	d02	d03	d01	d02	d03	
P (hPa)	869.6±2.6	835.3±2.5	827.6±2.4	801.3±2.4.6	801.3±2.4	801.4±2.4	801.1±2.4
Min/Max	862.8/875.1	828.3/840.8	821.2/833.1	795.0/806.7	795.0/806.7	795.2/806.8	795.1/806.8
T2 (°C)	22.3±1.8	20.4±1.8	19.8±1.1	18.4±0.8	18.4±0.9	18.3±0.9	19.5±1.1
Min/Max	16.2/28.7	15.1/26.0	14.0/25.0	16.1/20.9	15.5/21.8	15.6/22.1	14.8/25.6
RH2(%)	88.2±9.7	94.3±6.4	92.3±7.9	86.2±10.9	93.8±8.5	91.5±9.7	94.7±9.5
Min/Max	53.3/100	67.6/100	52.3/100	43.9/100	51.3/100	47.9/100	31.6/100
WS10 (ms ⁻¹)	2.1±1.1	3.0±1.4	2.6±1.7	3.4±2.6	4.8±3.1	4.0±3.1	2.1±1.4
Min/Max	0.0/8.6	0.1/11.4	0.1/11.7	0.0/20.2	0.1/23.9	0.1/22.1	0.0/10.0

379



380

381 **Figure 6:** Mean diurnal variations of (a) 2m temperature: T2, (b) 2m relative humidity: RH2, and (c) 10m
 382 wind speed: WS10 from model simulations (d01, d02 and d03) and observations. Altitude adjusted

383 variations are also shown (d–f). The bars represent the standard deviation and shown only for domain d01
384 and the observations in order to avoid the overlap.

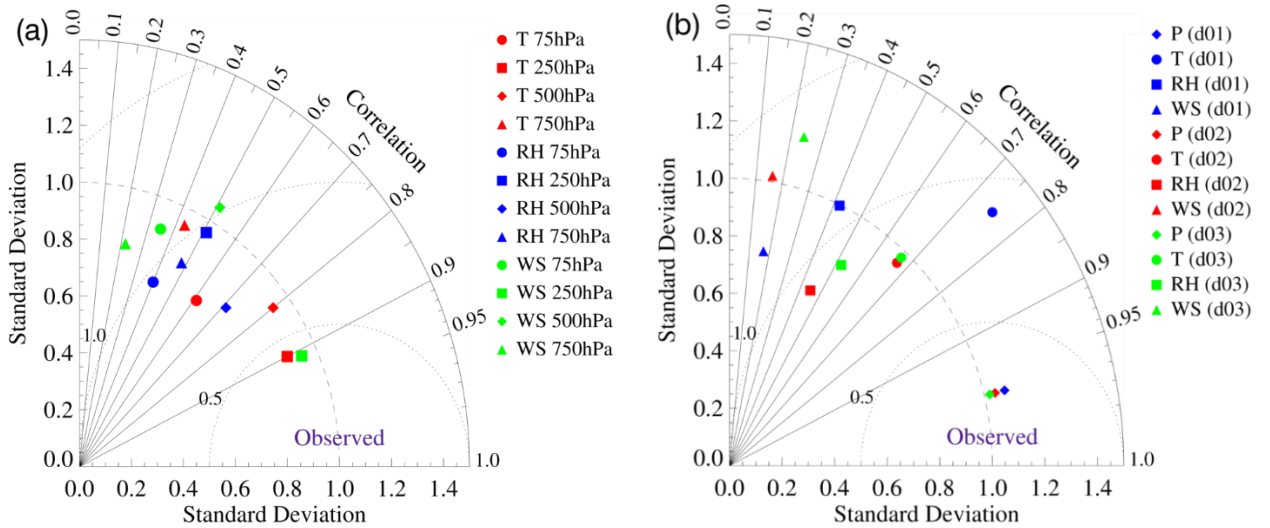
385

386 Due to the complex terrain and the grid size of the model, the simulated altitude of the observational site
387 could differ from reality. In this study, the model underestimated station altitude by about 588m, 480m,
388 and 270m in d01, d02, and d03. We performed an additional evaluation to explore and achieve the possible
389 improvement linearly interpolating the vertical profile of meteorological parameters to the actual altitude
390 of the station (Figure d-f), as done in a few previous study (e.g. Mues et al., 2018). The altitude adjustment
391 has been as per the equation of linear interpolation given in the supplementary material (equation - 4). The
392 analysis shows that the correlation coefficient values between model and observations do not show any
393 clear improvement (e.g. for T2 correlation coefficient is 0.35) on adjusting the altitude in model output
394 except for WS10. After adjusting the altitude, the temperature variability is suppressed by the model at
395 diurnal (Figure 6 a, d) and day to day timescales, i.e. r drops from 0.67 to 0.36 in d03. The comparison of
396 temperature among the three domains for additional model layers has also been analyzed (Figure S4). The
397 diurnal amplitudes are seen to be smaller at higher model layers. Additionally, the differences among
398 different simulations (d01, d02, and d03) also decrease at higher layers. As expected, the altitude
399 adjustment does reduce bias in pressure. Nevertheless, reductions in mean biases are not achieved (Table
400 S1); instead, absolute values of biases increase from 0.2 to 1.2, 2.4 to 3.1, 0.5 to 1.9, 0.7 to 1.6 in T2, RH2,
401 WS10, and Q2 in simulation d03. Besides thermal and mechanical interactions of the mountain surfaces
402 with atmosphere, local processes such as evaporation and transpiration affect the near-surface
403 meteorological conditions. A reduction in wind speed during the daytime is associated with the competing
404 effects of the mountain-valley circulations due to heating of the slopes versus synoptic-scale flows
405 (Solanki et al., 2019). To resolve such sub-grid scale processes, we emphasize that very high-resolution
406 simulations are needed as conducted in this study in order to simulate the meteorological variability in a
407 satisfactory way. The analysis further highlights a need of accurate representation of the complex

408 topographical features rather than altitude adjusted estimations which led to very limited improvements in
409 this case. However, we will discuss the evaluation without altitude adjustment until stated otherwise.

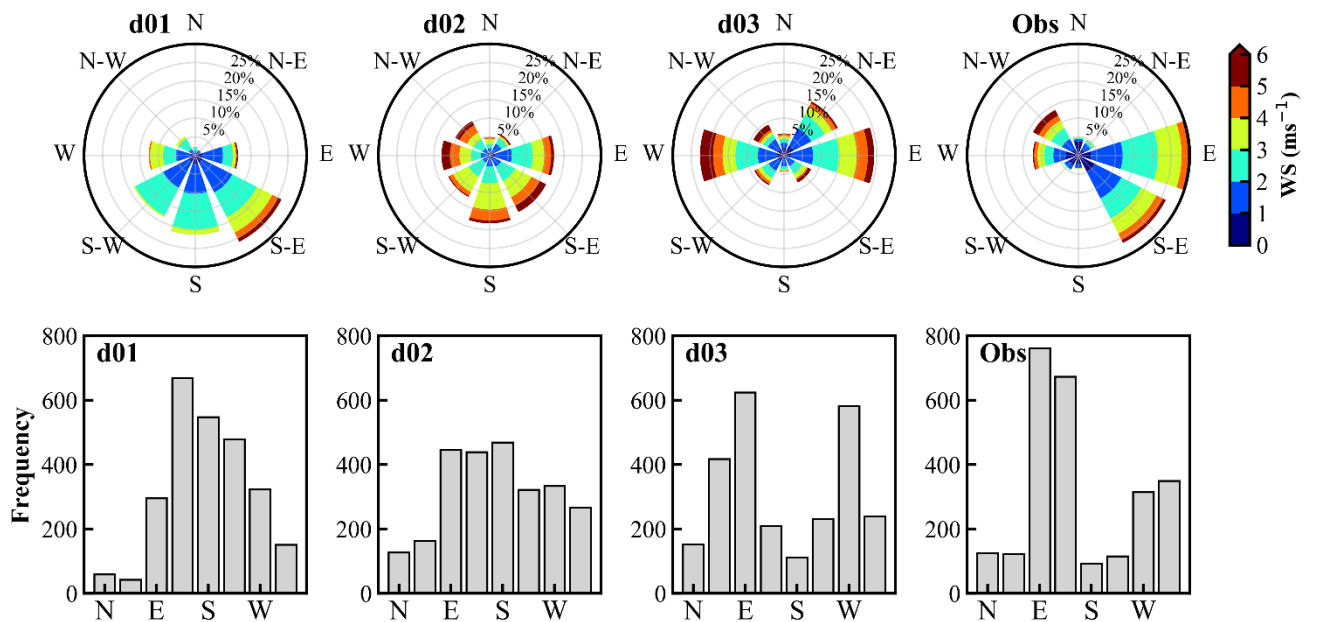
410 We evaluate the MB values (Table 1 and Table S1) in model simulations considering the benchmarks as
411 suggested by Emery et al (2001). In the d03 simulation, MB values for both T2 (0.2⁰C) and Q2 (-0.7 g kg⁻¹)
412 ¹) are found to be well within the range of benchmark values: ±0.5⁰C for T2 and ±1.0 g kg⁻¹ for Q2. It is
413 important to note that biases in T2 in the coarser simulations d01 (2.8⁰C) and d02 (0.9⁰C) are however
414 higher as compared to the benchmarks. MB values in T2 estimated, for this representative Himalayan site,
415 are found to be slightly lower (+0.2 ⁰C) (-1.2 ⁰C with altitude adjustment) than these over the Tibetan
416 Plateau (-2 to -5 ⁰C) (Gao et al., 2015) and over mountainous regions in the Europe (Zhang et al., 2013).
417 Warmer bias in our case is due to underestimation of the Himalayan altitude, whereas, model
418 overestimated terrain height over the Tibetan Plateau region giving contrasting results. Further, the RMSE
419 in wind speed is lower (1.6–2.0 ms⁻¹) than that over Kathmandu valley (2.2 ms⁻¹; Mues et al., 2018) and
420 similar to benchmark (2.0 ms⁻¹). Mar et al (2016) also reported akin bias (2 ms⁻¹) in the 10m wind speed
421 over Europe and the average correlation of ~0.4–0.6 over the Alps. Nevertheless, simulating the diurnal
422 variation of near-surface winds still remains challenging over complex terrain, but the bias was reduced
423 after including effects of the turbulent orographic form drag (Zhou et al., 2017; 2019). Besides turbulent
424 orographic form drag, it is suggested that wind speed is sensitive towards boundary layer schemes (Yver
425 et al., 2013; Zhou et al., 2019) and that more studies are needed to explore these aspects over the central
426 Himalaya.

427



428

429 **Figure 7:** Taylor diagram with the correlation coefficient, normalized standard deviation, and normalized
 430 root mean square difference (RMSD) error for (a) model performance at different pressure levels shown
 431 in Figure 3 for d01, and (b) the model simulated surface pressure, 2m temperature, RH and 10 m wind
 432 speed for different domains as shown in Figure 6a-c.



433

434

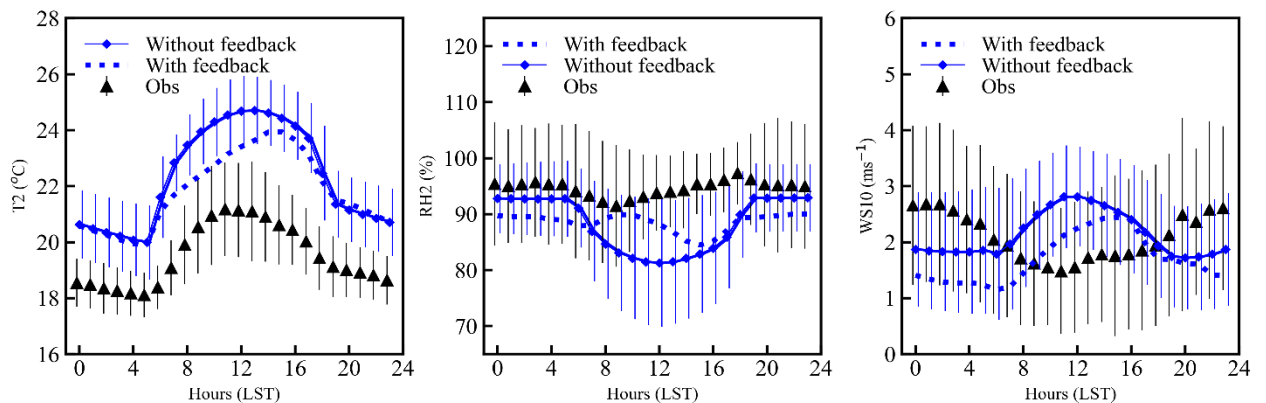
435 **Figure 8:** Comparison of the wind speed and direction represented by the wind rose (top panel), and
436 frequency distribution of wind direction (bottom panel) for model simulations over the three domains (d01,
437 d02, d03) and observations (obs) during June-September 2011. Different colours and radii of wind roses
438 show the wind speed and frequency of occurrences, respectively.

439
440 The wind direction is strongly influenced by the surrounding topography over the mountainous region and
441 the evaluation of the wind direction at horizontal resolution is depicted in Figure 8. The winds varying
442 between meteorological direction 337.5° and 22.5° are considered to be the Northerly and represented by
443 N in the frequency distribution and so on for other directional flow, referring to the clockwise
444 meteorological convention. The wind flow dominance over the observational site is easterly (30%) and
445 south-easterly (26%) while 26% occurrences of wind are from the west and north-west. The percentage of
446 southerly (21%) and south-westerly (SW, 19%) are relatively higher in d01 as compared to the
447 observations (S: 4% and SW: 5% respectively) and decreases to 4% and 9% in d03. Model is able to
448 simulate the northerly and north-easterly winds in d01 and d02, while, the model simulates larger
449 contribution of north-easterly and westerly winds in d03 which is not witnessed by the observations. The
450 easterly component of the model simulated wind shows better agreement with observations on increasing
451 the model resolution. In addition, the model is able to simulate the westerly and north-westerly wind
452 contribution in d02, whereas, the westerly component is overpredicted by 10 percentage points in d03.
453 The observations show that winds blowing from north, north-easterly, south and south-westerly are very
454 weak ($<2 \text{ ms}^{-1}$), and amount to be about $\sim 15\%$ of the total occurrences. The diurnal variation of the wind
455 direction is not investigated here, however the impact of mountain topography on the near surface flow
456 under low wind conditions has been discussed elsewhere (Solanki et al., 2019). Overall, the simulated
457 wind field in d03 is relatively in better agreement with observations than d01 and d02. This is further
458 assessed in section 3.5 using a finer resolution simulation by implementing SRTM 3s terrain data.

459

460 **3.4. Effect of feedback**

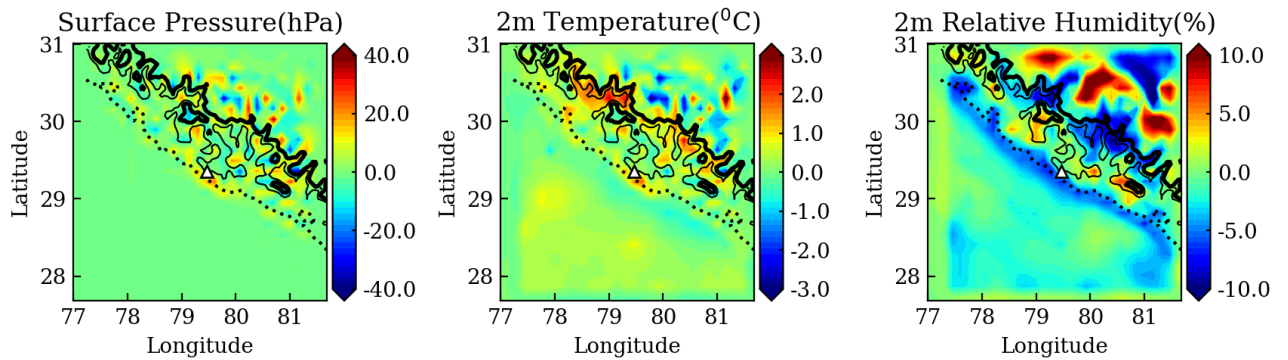
461 In the preceding section, the simulations were carried out without any feedback (WRF-WF) from the finer
 462 resolution domain to its parent domain, and results have been discussed. This WRF-WF experiment was
 463 conducted in such a way that it could explicitly account for the grid resolution effects on the model
 464 performance. The simulated meteorology with this model setup (with feedback) depicted different model
 465 performance in outermost coarse resolution domain d01 compared to d02 and d03. The model performance
 466 depends upon the boundary and initial conditions. Another model simulation is carried out in this section
 467 using the same configuration but with two-way interactive nesting and feedback (WRF-F) from nested
 468 domain to its parent domain. The simulated meteorological parameters in the higher nests, are fed back to
 469 its parent domains, and the boundary conditions replaced there. The model results over the CH region, in
 470 the regional scale simulation (d01), shows better agreement with the observations, because of the feedback
 471 from high resolution nested simulation. The comparison of the simulated meteorological parameters (T2,
 472 RH2, and WS10) for the outermost domain with the surface observations is presented in Figure 9 for both
 473 WRF-WF and WRF-F simulations thus showing the effect of the feedback within the outermost domain.



474 **Figure 9:** Diurnal variation of the T2, RH2, and WS10 from d01 without feedback (WRF-WF) and with
 475 feedback (WRF-F) simulations. The bars represent the standard deviation and shown only for domain d01
 476 and observations in order to avoid the overlap.

477 The comparison of mean values (Table 2) shows a decrease in model bias for T2, RH2, and Q2 by 0.5 °C,
 478 0.3%, and 0.2 g kg⁻¹ respectively due to feedback from finer resolution simulations. Additionally,

479 correlations are found to show improvements for RH2 and Q2 by 0.15 and 0.12, respectively, due to
 480 feedback, hence, the diurnal variation of relative humidity is more closer to the observation (Figure 9).
 481 Nevertheless, smaller changes were seen in correlations for WS10 (by 0.05) and T2 (by -0.02) (Figure S5).
 482 Variations in wind speed and direction also show significant improvements, especially in the dominant
 483 flow direction, e.g. easterly, westerly and north-westerly (Figure S6).



484
 485 **Figure 10:** The effect of the two-way nesting on d01 is shown. The difference between the simulations
 486 with feedback (WRF-F) and without feedback (WRF-WF) is shown for surface pressure, 2m temperature,
 487 and 2m relative humidity along with three elevation contours at 500m (dashed), 1500m (thin solid), and
 488 2000m (thick solid).

489 **Table 2:** Comparison of the simulated meteorology for surface pressure (P), 2m Temperature (T2), 2m
 490 relative humidity (RH2), 10m wind speed (WS10) and 2m specific humidity (Q2) in two model
 491 simulations: WRF-WF and WRF-F in the outermost domain d01 to the observations.

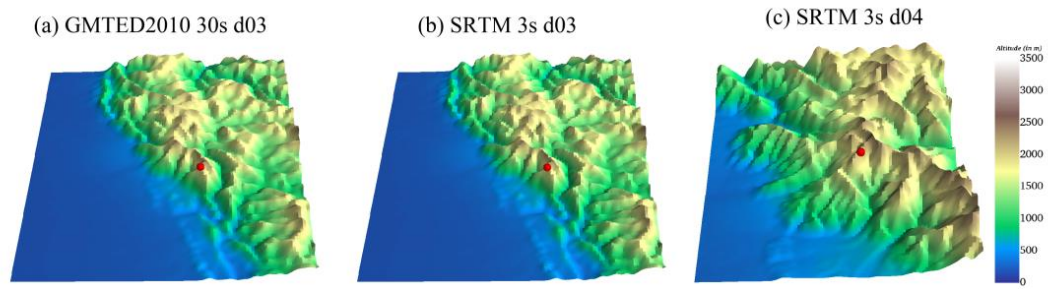
Parameters	Observed	WRF-WF	WRF-F
P (hPa)	801.4±2.4	869.6±2.6	858.9±2.5
T2 (°C)	19.5±1.6	22.3±2.1	21.9±1.4
RH2 (%)	94.7±9.5	88.2±4.9	88.6±4.9
WS10 (ms ⁻¹)	2.1±1.4	2.1±1.1	1.7±1.3
Q2(g kg ⁻¹)	16.8±2.0	17.3±2.0	17.0±2.1

492

493 Effects of the feedback on surface pressure, 2m temperature and relative humidity in the domain d01 are
494 shown by Figure 10. Feedback effects are seen to be more pronounced over the mountainous region than
495 over the flat terrain of the IGP. The feedback from the nested domain to the parent domain mostly modifies
496 the meteorology over the mountainous region, as shown by the topography contours in Figure 10. The
497 analyses of biases and correlations suggest an improvement in the model simulated pressure, temperature,
498 and humidity through feedback from well-resolved nests. This further underpins that better representations
499 of the Himalaya over local-scales can be adopted to simulate meteorology at the regional-scale with lower
500 biases over complex terrain in the given domain. Nevertheless, further modelling studies alongside with
501 more observations are needed to improve the model performance. We extended the efforts to improve the
502 wind speed and direction simulated over the complex topography by implementing a high resolution (3s)
503 topographical input in the model as to evaluate finer resolution features over the Himalaya in the following
504 section.

505 **3.5. Inclusion of high resolution (3s) SRTM topography**

506 Simulations described in previous sections were performed using the 30s (~1km) topographic data from
507 the GMTED2010 (Danielson and Gesch, 2011) which is comparable to the highest resolution of the WRF
508 simulation (d03). In order to evaluate the influences of topographical features on the wind flow at finer
509 scales, the topography input available at very high resolution (3s or ~90m) from the Shuttle Radar
510 Topography Mission (SRTM3s) (Farr et al., 2007) have been utilized. However, retaining the model
511 configuration same as earlier, an additional innermost nest d04 having a resolution of ~333m, as depicted
512 in Figure 1 (bottom right panel) is included. Simulation with SRTM data at 1 km resolution did not differ
513 significantly with the similar resolution simulation using GMTED2010 (GMTED hereafter). For this
514 experiment, model simulation is performed only for September 2011. This simulation is carried out
515 without feedback and compared with the observation to check the effect of implementing high-resolution
516 topography.



Red dot represents observational site Manora Peak

517

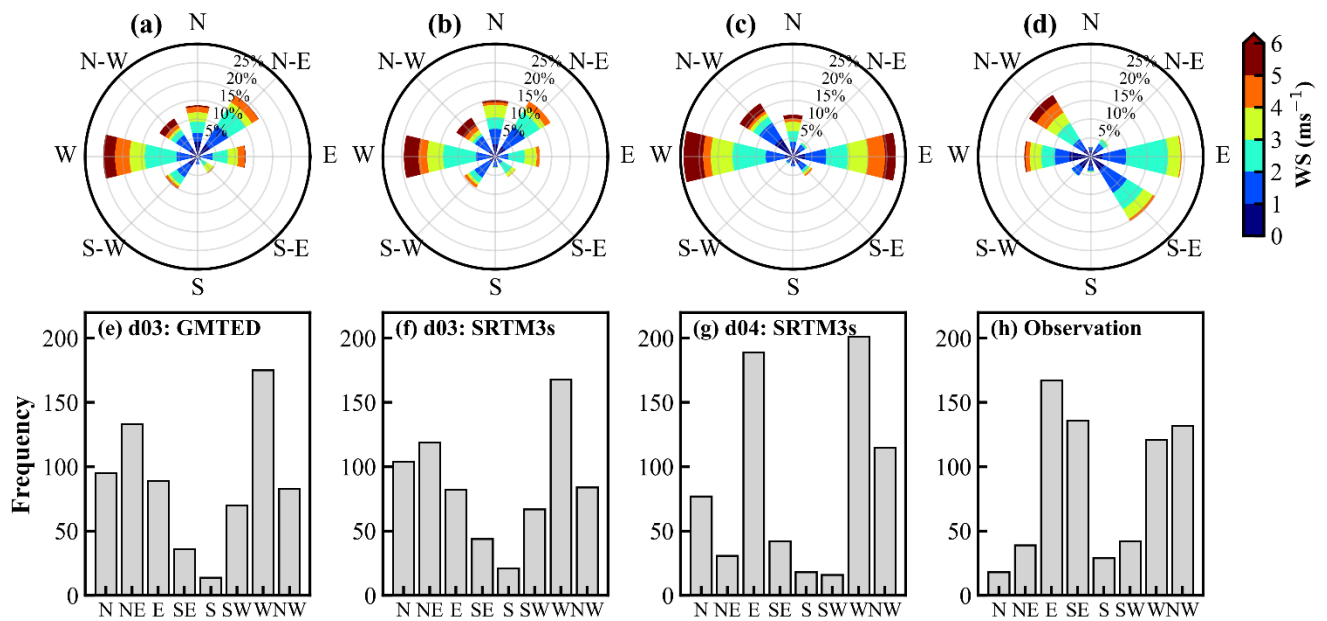
518 **Figure 11:** The topography from GMTED at 30s in domain d03 (a), SRTM at 3s in domain d03 (b) and
 519 SRTM at 3s in domain d04 (c). The model elevations of the observational site in d03 and d04 are 1670m
 520 and 1876m respectively.

521

522 The comparison of the topographic height between GMTED and SRTM3s, in Figure S7, shows that the
 523 differences are larger over the mountainous region, which vary from -100 to +100m. The differences are
 524 suppressed within d02 and d03 as the topography input is changed from GMTED to SRTM3s datasets.
 525 The topography in d04 (Figure 11c) gets resolved better, and marked by sharp variations of mountain
 526 ridges and valleys using the SRTM3s as compared to d03, which are smoothed out with GMTED (Figure
 527 11a) or with SRTM3s interpolated to 1 km (Figure 11b). After including the SRTM3s topography, the MB
 528 value for wind speed in d03 is found to show a slight reduction ($\sim 0.04 \text{ ms}^{-1}$). Also, the flow from various
 529 directions exhibited an improvement of 1-2% with the use of SRTM3s (Table S2).

530 In d04, surface pressure is seen to be simulated more realistically (809 hPa), and the dry bias in 2m relative
 531 humidity is improved by $\sim 2\%$ (Figure S8 and Table S2). Simulations of diurnal wind variations remain
 532 challenging (not shown here) even at finest resolutions considered (d04), even utilizing the updated
 533 topographic data (SRTM3s). Further, to understand the effect of SRTM3s data in d04, the wind direction
 534 is compared with that in d03 and observations. The variations in winds are analysed and shown by the
 535 wind rose (Figure 12a-d) and frequency distribution (Figure 12e-h). The fraction of north-easterly
 536 component in d04 with SRTM3s (5%) is found to be comparable with observations (6%), which was
 537 overestimated by 19% (17%) in d03 with GMTED (SRTM3s). The frequency of the southerlies improves

538 with the increasing resolution of topography and matches better with the observations. The observations
 539 show the prevalence of north-westerly (19%), easterly (24%), westerly (18%) and south-easterly (20%)
 540 winds and these are also seen to be dominant directions in the simulation d04 with the exception of south-
 541 easterly winds.



542
 543 **Figure 12:** Wind roses (a) d03 using GMTED, (b-c) d03 and d04 using SRTM3s topography data, and (d)
 544 surface observation. Corresponding frequency distribution of the wind directions are shown from e-f. The
 545 comparison of the wind speed and direction are shown for the month of September, 2011.

546
 547 Simulation of the wind directions improved from d03 to d04 by using the SRTM3s topography, except
 548 certain wind directions such as south-easterly. An improvement is noticed in simulated surface pressure,
 549 2 m relative humidity and 10 m wind speed using the SRTM3s topography. Topographical data at different
 550 resolutions is found to show the RH differences in the range of -1 to 1% in d02 and -3 to 3% in d03 (Figure
 551 S9). Differences in simulated RH could be associated with the multi-scale orographic variations which are
 552 found to be the key factors in meteorological simulation over complex terrain (e.g. Wang et al., 2020).
 553 The effects of the SRTM3s topographic static data have been studied previously over other regions of the
 554 world (e. g. Teixeira et al., 2014; De Meij and Vinuesa, 2014). However, the daytime lower wind speed

555 and the transition phases during morning and evening hours still remain a challenge even after using the
556 high resolution (333m x 333m) nest. Such discrepancies between model and observations over the
557 Himalayan region are suggested to be associated with still unresolved terrain features, besides the
558 influences of input meteorological fields as well as the model physics on simulated atmospheric flows (e.
559 g. Xue et al., 2014; Vincent et al., 2015).

560

561 **4. Summary and Conclusions**

562 This study using WRF-model mainly elucidated upon the various diagnostics it calculates for its multiple
563 domains, the comparison of model results to an intensive field campaign and downscaling to a sub-
564 kilometer resolution with 3s resolution SRTM topography data that resolves individual peaks and valleys
565 over the CH region. The effects of spatial resolution on model simulated meteorology have examined by
566 combining the WRF model with ground-based, and in-situ observations, and reanalysis datasets. Owing
567 to the highly complex topography of the central Himalaya, model results show strong sensitivity towards
568 the model resolution and adequate representation of terrain features. Model simulated meteorological
569 profiles do not show much dependency on the resolution, except in the lower atmosphere, which is directly
570 influenced by terrain induced effects and surface characteristics emphasizing the need to evaluate various
571 physics schemes over this region. The biases in 2 m temperature, relative humidity and surface pressure
572 show a decrease on increasing the model resolution indicating a better resolved representation of
573 topographical features. Diurnal variations in meteorological parameters also show better agreements on
574 increasing the grid resolution. Although the surface pressure does not show a pronounced diurnal variation,
575 nevertheless, the biases in simulated surface pressure reduce significantly over fine-resolution simulations.
576 Interpolation of coarser simulations (d01, d02) to the station altitude reduces the bias in surface pressure
577 and temperature, but suppresses the diurnal variability. The results highlight the significance of accurately
578 representing terrains at finer resolutions (d03). Model is generally not able to reproduce the frequency
579 distribution of wind direction, except in some of the major components in all the simulations with varying

580 resolutions. The directionality of the simulated winds shows improvements over finer grid resolutions;
581 however, reproducing the diurnal variability still remains a challenge. Biases are stronger typically during
582 daytime and also during transitions of low to high wind conditions and vice versa. This is attributed to the
583 uncertainties in representing the interaction of slope winds with the synoptic mean flow and local
584 circulations, despite an improved representation of terrain features. A sensitivity experiment with domain
585 feedback turned ON shows that the feedback process can improve the representation of the CH in the
586 simulation covering a larger region of the northern Indian subcontinent. It is suggested that further
587 improvements in the model performance are limited due to the lack of high-resolution topographical input
588 biases through input meteorological fields, and model physics. Nevertheless, the implementation of a very
589 high resolution (3s) topographical input using the SRTM data shows the potential to reduce the biases
590 related to topographical features to some extent.

591

592 **Code and data availability**

593 Observational data from the GVAX campaign is available freely
594 (<https://adc.arm.gov/discovery/#v/results/s/fsite::pgh.M>). WRF is an open-source and publicly available
595 model, which can be downloaded at http://www2.mmm.ucar.edu/wrf/users/download/get_source.html.
596 A zip file containing a) namelists for both pre-processor (WPS) as well as the WRF, b) 3s resolution
597 topography input prepared for the pre-processor, along with a README file describing the necessary
598 details to perform the simulations, has been archived at <https://doi.org/10.5281/zenodo.3978569>.

599

600 **Author contributions**

601 NS and AP designed and supervised the study. JS performed the simulations, assisted by NO and AS. JS,
602 NO, AS analysed the model results and NVPKK, KR, SSG contributed to the interpretations. VRK

603 contributed significantly in conceiving and realizing the GVAX campaign. JS and NS wrote the first draft,
604 and all the authors contributed to the manuscript.

605

606 **Acknowledgement**

607 This study has been supported by ABLN& C: NOBLE project under ISRO-GBP. We are thankful to
608 Director ARIES, Nainital. We acknowledge NCAR for the WRF-ARW model, ECMWF for the ERA-
609 Interim reanalysis data sets, ARM Climate Research Facility of U.S. Department of Energy (DOE) for the
610 observations made during the GVAX campaign. Computing resources from the Max Planck Computing
611 and Data Facility (MPCDF) are profoundly acknowledged. N. Ojha acknowledges the computing
612 resources - Vikram-100 HPC at Physical Research Laboratory (PRL), and valuable support from
613 Duggirala Pallamraju and Anil Bhardwaj. Constructive comments and suggestions from the anonymous
614 reviewers and the handling editor are gratefully acknowledged.

615

616 **References**

617 Angevine, W. M., Bazile, E., Legain, D. and Pino, D.: Land surface spinup for episodic modeling, *Atmos.*
618 *Chem. Phys.*, 14(15), 8165–8172, doi:10.5194/acp-14-8165-2014, 2014.

619 Bhutiyani, M.R., Kale, V.S. and Pawar, N.J.: Long-term trends in maximum, minimum and mean annual
620 air temperatures across the Northwestern Himalaya during the twentieth century. *Climatic Change*, 85, 59-
621 177, <https://doi.org/10.1007/s10584-006-9196-1>, 2007.

622 Bonasoni, P., Cristofanelli, P., Marinoni, A., Vuillermoz, E. and Adhikary, B.: Atmospheric pollution in
623 the Hindu Kush–Himalaya region: Evidence and implications for the regional climate. *Mountain research*
624 *and development*, 32, 468-479, 2012.

625 Boyle, J. and Klein, S.A.: Impact of horizontal resolution on climate model forecasts of tropical
626 precipitation and diabatic heating for the TWP-ICE period. *Journal of Geophysical Research:*
627 *Atmospheres*, 115, <https://doi.org/10.1029/2010JD014262>, 2010.

628 Cannon, F., Carvalho, L. M. V, Jones, C., Norris, J., Bookhagen, B. and Kiladis, G. N.: Effects of
629 topographic smoothing on the simulation of winter precipitation in High Mountain Asia, *J. Geophys. Res.*
630 *Atmos.*, 122(3), 1456–1474, doi:<https://doi.org/10.1002/2016JD026038>, 2017.

631 Caya, D. and Laprise, R.: A semi-implicit semi-Lagrangian regional climate model: The Canadian RCM.
632 *Monthly Weather Review*, 127, 341-362, [https://doi.org/10.1175/1520-
633 0493\(1999\)127<0341:ASISLR>2.0.CO;2](https://doi.org/10.1175/1520-0493(1999)127<0341:ASISLR>2.0.CO;2), 1999.

634 Chen, F. and Dudhia, J.: Coupling an advanced land surface–hydrology model with the Penn State–NCAR
635 MM5 modeling system. Part I: Model implementation and sensitivity. *Monthly Weather Review*, 129,
636 569-585, [https://doi.org/10.1175/1520-0493\(2001\)129<0569:CAALSH>2.0.CO;2](https://doi.org/10.1175/1520-0493(2001)129<0569:CAALSH>2.0.CO;2)2001.

637 Cheng, W. Y. Y. and Steenburgh, W. J.: Evaluation of surface sensible weather forecasts by the WRF and the Eta
638 Models over the western United States, *Weather Forecast.*, 20(5), 812–821, doi:10.1175/WAF885.1, 2005.

639 Chou, M.D. and Suarez, M.J.: An efficient thermal infrared radiation parameterization for use in general
640 circulation models, NASA Technical Memorandum No. 104606, Vol. 3, pp.85,1994.

641 Christensen, J.H., Christensen, O.B., Lopez, P., van Meijgaard, E. and Botzet, M.: The HIRHAM4
642 regional atmospheric climate model. DMI Scientific report, 4, p.51, 1996.

643 Danielson, J.J. and Gesch, D.B.: Global multi-resolution terrain elevation data 2010 (GMTED2010) (No.
644 2011-1073), US Geological Survey, 2011.

645 De Meij, A. and Vinuesa, J. F.: Impact of SRTM and Corine Land Cover data on meteorological
646 parameters using WRF, *Atmos. Res.*, 143, 351–370, doi:10.1016/j.atmosres.2014.03.004, 2014.

647 Dee, D.P., Uppala, S.M., Simmons, A.J., Berrisford, P., Poli, P., Kobayashi, S., Andrae, U., Balmaseda,
648 M.A., Balsamo, G., Bauer, D.P. and Bechtold, P.: The ERA-Interim reanalysis: Configuration and
649 performance of the data assimilation system. *Quarterly Journal of the royal meteorological society*, 137,
650 pp.553-597, <https://doi.org/10.1002/qj.828>, 2011.

651 Deep, A., Pandey, C.P., Nandan, H. et al. Evaluation of ambient air quality in Dehradun city during 2011–
652 2014. *J Earth Syst Sci* 128, 96, doi:10.1007/s12040-019-1092-y, 2019.

653 Dimri, A.P., Chevuturi, A., Niyogi, D., Thayyen, R.J., Ray, K., Tripathi, S.N., Pandey, A.K. and Mohanty,
654 U.C.: Cloudbursts in Indian Himalayas: a review. *Earth-science reviews*, 168, pp.1-23,
655 <https://doi.org/10.1016/j.earscirev.2017.03.006>, 2017.

656 Dumka, U. C., Kaskaoutis, D. G., Sagar, R., Chen, J., Singh, N. and Tiwari, S.: First results from light
657 scattering enhancement factor over central Indian Himalayas during GVAX campaign, *Sci. Total Environ.*,
658 605–606, 124–138, doi:<https://doi.org/10.1016/j.scitotenv.2017.06.138>, 2017.

659 Ek, M.B., Mitchell, K.E., Lin, Y., Rogers, E., Grunmann, P., Koren, V., Gayno, G. and Tarpley, J.D.:
660 Implementation of Noah land surface model advances in the National Centers for Environmental
661 Prediction operational mesoscale Eta model. *Journal of Geophysical Research: Atmospheres*,
662 <https://doi.org/10.1029/2002JD003296>, 2003.

663 Emery, C., Tai, E., and Yarwood, G.: Enhanced meteorological modeling and performance evaluation for two Texas
664 ozone episodes, Tech. Rep. Prepared for The Texas Natural Resource Conservation Commission, ENVIRON
665 International Corporation, 2001.

666 Farr, T.G., Rosen, P.A., Caro, E., Crippen, R., Duren, R., Hensley, S., Kobrick, M., Paller, M., Rodriguez,
667 E., Roth, L. and Seal, D.: The shuttle radar topography mission, *Reviews of geophysics*, 45(2).
668 doi:10.1029/2005RG000183, 2007.

669 Foley, A.M.: Uncertainty in regional climate modelling: A review. *Progress in Physical Geography*, 34,
670 pp.647-670.<https://doi.org/10.1177/0309133310375654>, 2010.

671 Gao, Y., Xu, J. and Chen, D.: Evaluation of WRF mesoscale climate simulations over the Tibetan Plateau during
672 1979-2011, *J. Clim.*, 28(7), 2823–2841, doi:10.1175/JCLI-D-14-00300.1, 2015.

673 Hanna, S. R. and Yang, R.: Evaluations of Mesoscale Models' Simulations of Near-Surface Winds, Temperature
674 Gradients, and Mixing Depths, *J. Appl. Meteorol.*, 40(6), 1095–1104, doi:10.1175/1520-
675 0450(2001)040<1095:EOMMSO>2.0.CO;2, 2001.

676 Hong, S.Y., Noh, Y. and Dudhia, J.: A new vertical diffusion package with an explicit treatment of
677 entrainment processes. *Monthly weather review*, 134, pp.2318-2341,
678 <https://doi.org/10.1175/MWR3199.1>, 2006.

679 Jerez, S., López-Romero, J. M., Turco, M., Lorente-Plazas, R., Gómez-Navarro, J. J., Jiménez-Guerrero,
680 P. and Montávez, J. P.: On the Spin-Up Period in WRF Simulations Over Europe: Trade-Offs Between
681 Length and Seasonality, *J. Adv. Model. Earth Syst.*, 12(4), e2019MS001945,
682 doi:<https://doi.org/10.1029/2019MS001945>, 2020.

683 Kain, J.S.: The Kain–Fritsch convective parameterization: an update. *Journal of applied meteorology*, 43,
684 pp.170-181, [https://doi.org/10.1175/1520-0450\(2004\)043<0170:TKCPAU>2.0.CO;2](https://doi.org/10.1175/1520-0450(2004)043<0170:TKCPAU>2.0.CO;2), 2004.

685 Kotamarthi, V.R.: Ganges Valley Aerosol Experiment (GVAX) Final Campaign Report. DOE/SC-ARM-
686 14-011, available at: <https://www.arm.gov/publications/programdocs/doe-sc-arm-14-011>. Pdf, 2013.

687 Kumar, A., Singh, N., Anshumali and Solanki, R.: Evaluation and utilization of MODIS and CALIPSO
688 aerosol retrievals over a complex terrain in Himalaya, *Remote Sens. Environ.*, 206(December 2017), 139–
689 155, doi:10.1016/j.rse.2017.12.019, 2018.

690 Kumar, R., Naja, M., Pfister, G.G., Barth, M.C. and Brasseur, G.P.: Simulations over South Asia using
691 the Weather Research and Forecasting model with Chemistry (WRF-Chem): set-up and meteorological
692 evaluation. *Geoscientific Model Development*, 5, p.321, <https://doi.org/10.5194/gmd-5-321-2012>, 2012.

693 Laprise, R. Regional climate modelling. *Journal of Computational Physics*, 227, pp.3641-3666.,
694 <https://doi.org/10.1016/j.jcp.2006.10.024>, 2008.

695 Lawrence, M.G. and Lelieveld, J.: Atmospheric pollutant outflow from southern Asia: a review.
696 *Atmospheric Chemistry and Physics*, 10, p.11017, <https://doi.org/10.5194/acp-10-11017-2010>, 2010.

697 Lee, T. J., Pielke, R. A., Kessler, R. C. and Weaver, J.: Influence of Cold Pools Downstream of Mountain Barriers
698 on Downslope Winds and Flushing, *Mon. Weather Rev.*, 117(9), 2041–2058, doi:10.1175/1520-
699 0493(1989)117<2041:IOCPDO>2.0.CO;2, 1989.

700 Lelieveld, J., Bourtsoukidis, E., Brühl, C., Fischer, H., Fuchs, H., Harder, H., Hofzumahaus, A., Holland,
701 F., Marno, D., Neumaier, M. and Pozzer, A.: The South Asian monsoon—pollution pump and purifier.
702 *Science*, 361, pp.270-273, DOI:10.1126/science.aar2501, 2018.

703 Mar, K. A., Ojha, N., Pozzer, A. and Butler, T. M.: Ozone air quality simulations with WRF-Chem (v3.5.1) over
704 Europe: Model evaluation and chemical mechanism comparison, *Geosci. Model Dev.*, 9(10), 3699–3728,
705 doi:10.5194/gmd-9-3699-2016, 2016.

706 Meher, J.K., Das, L., Akhter, J., Benestad, R.E. and Mezghani, A.: 2017. Performance of CMIP3 and
707 CMIP5 GCMs to simulate observed rainfall characteristics over the Western Himalayan region. *Journal of*
708 *Climate*, 30, pp.7777-7799, <https://doi.org/10.1175/JCLI-D-16-0774.1>, 2017.

709 Mlawer, E.J., Taubman, S.J., Brown, P.D., Iacono, M.J. and Clough, S.A.: Radiative transfer for
710 inhomogeneous atmospheres: RRTM, a validated correlated-k model for the longwave. *Journal of*
711 *Geophysical Research: Atmospheres*, 102, pp.16663-16682. <https://doi.org/10.1029/97JD00237>, 1997.

712 Mues, A., Lauer, A., Lupascu, A., Rupakheti, M., Kuik, F. and Lawrence, M.G.: WRF and WRF-Chem
713 v3. 5.1 simulations of meteorology and black carbon concentrations in the Kathmandu Valley.
714 *Geoscientific Model Development*, 11, p.2067. <https://doi.org/10.5194/gmd-11-2067-2018>, 2018.

715 Naja, M., Bhardwaj, P., Singh, N., Kumar, P., Kumar, R., Ojha, N., Sagar, R., Satheesh, S. K., Krishna
716 Moorthy, K., Kotamarthi, V. R., High-frequency vertical profiling of meteorological parameters using
717 AMF1 facility during RAWEX–GVAX at ARIES, Nainital, *Current Science*, Vol. 111, No. 1, 132–140,
718 2016.

719 Nandargi, S. and Dhar, O.N.: Extreme rainstorm events over the northwest Himalayas during 1875–2010.
720 *Journal of Hydrometeorology*, <https://doi.org/10.1175/JHM-D-12-08.1> ,2012.

721 Norris, J., Carvalho, L. M. V, Jones, C. and Cannon, F.: Warming and drying over the central Himalaya
722 caused by an amplification of local mountain circulation, *npj Clim. Atmos. Sci.*, 3(1), 1,
723 doi:10.1038/s41612-019-0105-5, 2020.

724 Ojha, N., Girach, I., Sharma, K., Nair, P., Singh, J., Sharma, N., Singh, N., Flemming, J., Inness, A. and
725 Subrahmanyam, K.V.: Surface ozone in the Doon Valley of the Himalayan foothills during spring.
726 *Environ. Sci. Poll. Res.*, doi:10.1007/s11356-019-05085-2, 2019

727 Ojha, N., Naja, M., Singh, K.P., Sarangi, T., Kumar, R., Lal, S., Lawrence, M.G., Butler, T.M. and
728 Chandola, H.C.: Variabilities in ozone at a semi-urban site in the Indo-Gangetic Plain region: Association
729 with the meteorology and regional processes. *Journal of Geophysical Research: Atmospheres*,
730 <https://doi.org/10.1029/2012JD017716>, 2012.

731 Ojha, N., Pozzer, A., Rauthe-Schöch, A., Baker, A.K., Yoon, J., Brenninkmeijer, C.A. and Lelieveld, J.:
732 Ozone and carbon monoxide over India during the summer monsoon: regional emissions and transport.
733 *Atmos. Chem. Phys*, <https://doi.org/10.5194/acp-16-3013-2016>, 2016.

734 Pant, G.B., Pradeep Kumar, P., V. Revadekar, Jayashree, Singh, Narendra.: *The Himalaya*.
735 <https://doi.org/10.1007/978-3-319-61654-4>, 2018.

736 Pervez, M.S. and Henebry, G.M.: Projections of the Ganges–Brahmaputra precipitation—Downscaled
737 from GCM predictors. *Journal of Hydrology*, 517, pp.120-
738 134.<https://doi.org/10.1016/j.jhydrol.2014.05.016>, 2014.

739 Potter, E. R., Orr, A., Willis, I. C., Bannister, D. and Salerno, F.: Dynamical Drivers of the Local Wind
740 Regime in a Himalayan Valley, *J. Geophys. Res. Atmos.*, 123(23), 13,113-186,202,
741 doi:<https://doi.org/10.1029/2018JD029427>, 2018.

742 Rupakheti, D., Adhikary, B., Praveen, P.S., Rupakheti, M., Kang, S., Mahata, K.S., Naja, M., Zhang, Q.,
743 Panday, A.K. and Lawrence, M.G., 2017.: Pre-monsoon air quality over Lumbini, a world heritage site

744 along the Himalayan foothills. *Atmos. Chem. Phys.*, 17, 11041-11063, <https://doi.org/10.5194/acp-17->
745 11041-2017, 2017.

746 Sarangi, T., Naja, M., Ojha, N., Kumar, R., Lal, S., Venkataramani, S., Kumar, A., Sagar, R. and Chandola,
747 H.C.: First simultaneous measurements of ozone, CO, and NO_y at a high-altitude regional representative
748 site in the central Himalayas. *Journal of Geophysical Research: Atmospheres*, 119, pp.1592-1611.
749 <https://doi.org/10.1002/2013JD020631>, 2014.

750 Seck, A., Welty, C. and Maxwell, R. M.: Spin-up behavior and effects of initial conditions for an integrated
751 hydrologic model, *Water Resour. Res.*, 51(4), 2188–2210, doi:<https://doi.org/10.1002/2014WR016371>,
752 2015.

753 Sharma, A., Ojha, N., Pozzer, A., Mar, K. A., Beig, G., Lelieveld, J., and Gunthe, S. S.: WRF-Chem
754 simulated surface ozone over south Asia during the pre-monsoon: effects of emission inventories and
755 chemical mechanisms, *Atmos. Chem. Phys.*, 17, 14393–14413, <https://doi.org/10.5194/acp-17-14393->
756 2017, 2017.

757 Sharma, S.S. and Ganju, A.: Complexities of avalanche forecasting in Western Himalaya—an
758 overview. *Cold Regions Science and Technology*, 31, pp.95-102.<https://doi.org/10.1016/S0165->
759 232X(99)00034-8, 2000.

760 Singh, N., Solanki, R., Ojha, N., Janssen, R.H., Pozzer, A. and Dhaka, S.K.: Boundary layer evolution
761 over the central Himalayas from radio wind profiler and model simulations. *Atmospheric Chemistry &*
762 *Physics*, <https://doi.org/10.5194/acp-16-10559-2016>, 2016.

763 Skamarock, W. C., Klemp, J.B., Dudhia, J., Gill, D.O., Barker, D.M., Wang, W. and Powers, J.G.: A
764 Description of the Advanced Research WRF Version 3. NCAR Technical Note NCAR/TN-475+STR,
765 <http://dx.doi.org/10.5065/D68S4MVH>, 2008.

766 Solanki, R., Singh, N., Kumar, N.K., Rajeev, K. and Dhaka, S.K.: Time variability of surface-layer
767 characteristics over a mountain ridge in the central Himalayas during the spring season. *Boundary-layer*
768 *meteorology*, 158, pp.453-471, <https://doi.org/10.1007/s10546-015-0098-5>, 2016.

769 Solanki, R., Singh, N., Kiran Kumar, N. V. P., Rajeev, K., Imasu, R. and Dhaka, S. K.: Impact of
770 Mountainous Topography on Surface-Layer Parameters During Weak Mean-Flow Conditions, *Boundary-*
771 *Layer Meteorol.*, 172(1), 133–148, doi:10.1007/s10546-019-00438-3, 2019.

772 Srivastava, A. K., Soni, V. K., Singh, S., Kanawade, V. P., Singh, N., Tiwari, S. and Attri, S. D.: An early
773 South Asian dust storm during March 2012 and its impacts on Indian Himalayan foothills: A case study,
774 *Sci. Total Environ.*, 493, 526–534, doi:<https://doi.org/10.1016/j.scitotenv.2014.06.024>, 2014.

775 Sun, X.B., Ren, G.Y., Shrestha, A.B., Ren, Y.Y., You, Q.L., Zhan, Y.J., Xu, Y. and Rajbhandari, R.:
776 Changes in extreme temperature events over the Hindu Kush Himalaya during 1961–2015. *Advances in*
777 *Climate Change Research*, <https://doi.org/10.1016/j.accre.2017.07.001>, 2017.

778 Taylor, K.E.: Summarizing multiple aspects of model performance in a single diagram. *Journal of*
779 *Geophysical Research: Atmospheres*, 106, pp.7183-7192, <https://doi.org/10.1029/2000JD900719>, 2001.

780 Teixeira, J. C., Carvalho, A. C., Carvalho, M. J., Luna, T. and Rocha, A.: Sensitivity of the WRF model
781 to the lower boundary in an extreme precipitation event-Madeira island case study, *Nat. Hazards Earth*
782 *Syst. Sci.*, 14(8), 2009–2025, doi:10.5194/nhess-14-2009-2014, 2014.

783 Tewari, M., Chen, F., Wang, W., Dudhia, J., LeMone, M.A., Mitchell, K., Ek, M., Gayno, G., Wegiel, J.
784 and Cuenca, R.H.: Implementation and verification of the unified NOAA land surface model in the WRF
785 model. In 20th conference on weather analysis and forecasting/16th conference on numerical weather
786 prediction (Vol. 1115) , 2004,

787 Thompson, G., Rasmussen, R.M. and Manning, K.: Explicit forecasts of winter precipitation using an
788 improved bulk microphysics scheme. Part I: Description and sensitivity analysis. *Monthly Weather*
789 *Review*, 132(2), pp.519-542,[https://doi.org/10.1175/1520-0493\(2004\)132<0519:EFOWPU>2.0.CO;2](https://doi.org/10.1175/1520-0493(2004)132<0519:EFOWPU>2.0.CO;2),
790 2004.

791 Tiwari, P.R., Kar, S.C., Mohanty, U.C., Dey, S., Sinha, P. and Shekhar, M.S.: Sensitivity of the Himalayan
792 orography representation in simulation of winter precipitation using Regional Climate Model (RegCM)
793 nested in a GCM. *Climate Dynamics*, 49(11-12), pp.4157-4170, [https://doi.org/10.1007/s00382-017-](https://doi.org/10.1007/s00382-017-3567-3)
794 [3567-3](https://doi.org/10.1007/s00382-017-3567-3), 2017.

795 Tselioudis, G., Douvis, C. and Zerefos, C.: Does dynamical downscaling introduce novel information in
796 climate model simulations of precipitation change over a complex topography region? *International*
797 *Journal of Climatology*, 32, pp.1572-1578,<https://doi.org/10.1002/joc.2360>, 2012.

798 Vincent, C. L. and Hahmann, A. N.: The impact of grid and spectral nudging on the variance of the near-
799 surface wind speed, *J. Appl. Meteorol. Climatol.*, 54(5), 1021–1038, doi:10.1175/JAMC-D-14-0047.1,
800 2015.

801 Wang, Y., Leung, L.R., McGREGOR, J.L., Lee, D.K., Wang, W.C., Ding, Y. and Kimura, F.: Regional
802 climate modeling: progress, challenges, and prospects. *Journal of the Meteorological Society of Japan*.
803 Ser. II, 82, pp.1599-1628, <https://doi.org/10.2151/jmsj.82.1599>, 2004.

804 Wang, Y., Yang, K., Zhou, X., Chen, D., Lu, H., Ouyang, L., Chen, Y., Lazhu and Wang, B.: Synergy of orographic
805 drag parameterization and high resolution greatly reduces biases of WRF-simulated precipitation in central
806 Himalaya, *Clim. Dyn.*, 54(3), 1729–1740, doi:10.1007/s00382-019-05080-w, 2020.

807 Weisman, M.L., Skamarock, W.C. and Klemp, J.B.: The resolution dependence of explicitly modeled
808 convective systems. *Monthly Weather Review*, 125, pp.527-548, <https://doi.org/10.1175/1520->
809 0493(1997)125<0527:TRDOEM>2.0.CO;2, 1997.

810 Wilby, R.L., Hay, L.E. and Leavesley, G.H.: A comparison of downscaled and raw GCM output:
811 implications for climate change scenarios in the San Juan River basin, Colorado. *Journal of Hydrology*,
812 225, pp.67-91, [https://doi.org/10.1016/S0022-1694\(99\)00136-5](https://doi.org/10.1016/S0022-1694(99)00136-5), 1999.

813 Xue, Y., Janjic, Z., Dudhia, J., Vasic, R. and De Sales, F.: A review on regional dynamical downscaling
814 in intraseasonal to seasonal simulation/prediction and major factors that affect downscaling ability, *Atmos.*
815 *Res.*, 147–148, 68–85, doi:10.1016/j.atmosres.2014.05.001, 2014.

816 Yver, C. E., Graven, H. D., Lucas, D. D., Cameron-Smith, P. J., Keeling, R. F. and Weiss, R. F.: Evaluating transport
817 in the WRF model along the California coast, *Atmos. Chem. Phys.*, 13(4), 1837–1852, doi:10.5194/acp-13-1837-
818 2013, 2013.

819 Zadra, A., Caya, D., Côté, J.E.A.N., Dugas, B., Jones, C., Laprise, R., Winger, K. and Caron, L.P.: The
820 next Canadian regional climate model. *PhysCan*, 64, pp.75-83, 2008.

821 Zhang, D. L. and Zheng, W. Z.: Diurnal cycles of surface winds and temperatures as simulated by five boundary
822 layer parameterizations, *J. Appl. Meteorol.*, 43(1), 157–169, doi:10.1175/1520-
823 0450(2004)043<0157:DCOSWA>2.0.CO;2, 2004.

824 Zhang, Y., Sartelet, K., Wu, S. Y. and Seigneur, C.: Application of WRF/Chem-MADRID and WRF/Polyphemus
825 in Europe - Part 1: Model description, evaluation of meteorological predictions, and aerosol-meteorology
826 interactions, *Atmos. Chem. Phys.*, 13(14), 6807–6843, doi:10.5194/acp-13-6807-2013, 2013.

827 Zhou, X., Beljaars, A., Wang, Y., Huang, B., Lin, C., Chen, Y. and Wu, H.: Evaluation of WRF Simulations With
828 Different Selections of Subgrid Orographic Drag Over the Tibetan Plateau, *J. Geophys. Res. Atmos.*, 122(18), 9759–
829 9772, doi:10.1002/2017JD027212, 2017.

830 Zhou, X., Yang, K. and Wang, Y.: Implementation of a turbulent orographic form drag scheme in WRF and its
831 application to the Tibetan Plateau, *Clim. Dyn.*, 50(7–8), 2443–2455, doi:10.1007/s00382-017-3677-y, 2018.

832 Zhou, X., Yang, K., Beljaars, A., Li, H., Lin, C., Huang, B. and Wang, Y.: Dynamical impact of parameterized
833 turbulent orographic form drag on the simulation of winter precipitation over the western Tibetan Plateau, *Clim.*
834 *Dyn.*, 53(1–2), 707–720, doi:10.1007/s00382-019-04628-0, 2019.